Journal of Computational Physics (2020)

Contents lists available at ScienceDirect

Journal of Computational Physics

journal homepage: www.elsevier.com/locate/jcp

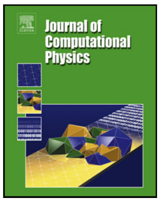

Analysis of geometric uncertainties in CFD problems solved by RBF-FD meshless method

Riccardo Zamolo[a,*], Lucia Parussini[a]

[a] *Department of Engineering and Architecture, University of Trieste, Via Valerio 10, 34127 Trieste, Italy*

A R T I C L E I N F O

Article history:
Received -
Received in final form -
Accepted -
Available online -

2000 MSC: 65N06, 60G15, 76D05, 35J25

Keywords:
Meshless
RBF-FD
Uncertainty
Polynomial chaos
Elliptic PDEs
Navier-Stokes

A B S T R A C T

In order to analyze incompressible and laminar fluid flows in presence of geometric uncertainties on the boundaries, the Non-Intrusive Polynomial Chaos method is employed, which allows the use of a deterministic fluid dynamic solver. The quantification of the fluid flow uncertainties is based on a set of deterministic response evaluations, which are obtained through a Radial Basis Function-generated Finite Differences meshless method. The use of such deterministic solver represents the key point of the analysis, thanks to the computational efficiency and similar accuracy over the traditional mesh-based numerical methods. The validation of the proposed approach is carried out through the solution of the flow past a $2D$ spinning cylinder near a moving wall and the flow over a backward-facing step, in presence of stochastic geometries. The applicability to practical problems is demonstrated through the investigation of geometric uncertainty effects on the forced convection of Al_2O_3-water nanofluid laminar flow in a grooved microchannel.

1. Introduction

In engineering applications, where manufacturing tolerances can significantly influence the performances, a specific attention must be paid to the analysis of geometric uncertainty effect during the components' design phase. Hence, the need of a methodology to deal with differential problems where the geometrical domain is treated as stochastic phenomenon.

There is a large literature on numerical methods to face problems with uncertain input parameters. We may find engineering applications of these methodologies exploring random material properties, random boundary conditions and/or random domain topology: [1, 2, 3, 4, 5, 6, 7, 8, 9, 10, 11, 12, 13, 14] just to mention some.

---

*Corresponding author.
e-mail: `rzamolo@units.it` (Riccardo Zamolo)

When non-intrusive techniques, such as the Non-Intrusive Polynomial Chaos (PC) method [15], are employed, the calculation of the random response is based on a set of deterministic response evaluations. So that, any available deterministic numerical solver can be used as a black box to quantify the effect of uncertainty. The only requirement is the solver to be sensitive to small variations of the stochastic parameters, because the response has to be computed at different, in general very close, values of these parameters.

When geometric uncertainty analysis is carried out, care should be taken using traditional mesh-based numerical methods to solve the deterministic problem, because it is well known that the numerical simulation can be mesh-dependent and the results are sensitive to the quality of the remeshing operation. Examples of CFD problems with geometric uncertainties, solved by non-intrusive techniques with remeshing of geometry (body-fitted approach) can be found in [6, 7, 14].

To override these problems, i.e. the mesh-dependency and the remeshing of geometries, in [9, 10, 11] a Polynomial Chaos methodology coupled to a Fictitious Domain solver has been presented. In the Fictitious Domain method, problems formulated on a complex domain can be solved on a simple-shaped Fictitious Domain containing the original one. In this way the computational domain of state problem, i.e. the Fictitious Domain, is independent by small variations of the stochastic physical domain boundaries, which are now immersed into the computational domain. Being the computational domain independent from random geometric parameters, the remeshing is not needed when the domain geometry changes.

With similar intent, in this paper the capabilities of the approach based on the coupling of Polynomial Chaos methodology and Radial Basis Function-generated Finite Differences (RBF-FD) meshless method are investigated. The main advantages of the RBF-FD meshless method over mesh-based methods are the geometric flexibility and the ability to easily deal with general and complex-shaped domains, since a simple distribution of nodes over the domain is required only, and no mesh/grid/tessellation is needed [16, 17]. Furthermore, the order of accuracy of RBF-FD methods can be easily increased by using larger stencils, i.e., more nodes in the local RBF expansion [18, 19, 20]. For these reasons the use of RBF-FD methods for the solution of partial differential equations (PDEs) is becoming more and more popular [21, 22], including the solution of fluid-flow problems [23, 24, 25, 26, 27, 28].

The validation of the proposed approach for the uncertainty quantification, Non-Intrusive PC and RBF-FD meshless method, is carried out through the solution of the Wannier flow in presence of random geometric parameters. Further analysis has been conducted on a representative model for which benchmark solutions exist, i.e the flow over a backward-facing step. In particular the effects of the presence of perpendicularity tolerances on the step have been examined. To better describe the advantages of the proposed approach, based one the use of RBF-FD meshless method, the obtained results are compared to those accomplished by a body-fitted approach, using the open source OpenFOAM code, based on finite volume method.

The applicability to practical problems is demonstrated through the investigation of geometric uncertainty effects on the forced convection of Al_2O_3-water nanofluid laminar flow in a grooved microchannel, showing the possibility to extend the methodology to industrial scale applications.

This paper is organized as follows: in the next section the governing equations of the thermo-fluid dynamic problems under analysis are given, in particular the details of the solution procedure are illustrated. In Section 3 the proposed methodology based on the Non-intrusive Polynomial Chaos and the RBF-FD meshless solver used to compute the deterministic flow field solutions is introduced. In Section 4 there are the validation and application of the proposed approach and in 5 a discussion on the achieved results is presented.

2. Governing equations and solution procedure

2.1. Governing equations

Let us consider a domain Ω filled with a fluid characterized by the following constant thermophysical properties: density ρ, kinematic viscosity ν, thermal diffusivity α and thermal conductivity k. The flow is considered incompressible, the viscous dissipation term in the energy equation is neglected and buoyancy effects are not considered. Under these hypotheses the conservation equations of mass, momentum and energy, in nondimensional form, are

$$\nabla \cdot \mathbf{u} = 0, \tag{1}$$

$$\frac{\partial \mathbf{u}}{\partial t} + (\mathbf{u} \cdot \nabla)\mathbf{u} = -\nabla p + \frac{1}{\mathrm{Re}}\nabla^2 \mathbf{u}, \tag{2}$$

$$\frac{\partial T}{\partial t} + \mathbf{u} \cdot \nabla T = \frac{1}{\mathrm{Re\ Pr}}\nabla^2 T. \tag{3}$$

In the above equations, length, velocity $\mathbf{u} = (u, v)$, time t, pressure p and temperature T are made nondimensional by taking H, U_0, H/U_0, ρU_0^2 and ΔT as reference quantities, respectively. $\mathrm{Re} = U_0 H/\nu$ is the flow Reynolds number and $\mathrm{Pr} = \nu/\alpha$ is the Prandtl number. The unsteady formulation of Eqs. (2)-(3) has been preferred over the steady formulation, i.e., without the time derivative terms, in order to enhance the convergence to the steady-state solutions, especially for high Re numbers involving slow decaying oscillations of the flow. These oscillations are more effectively dampened using the unsteady formulation because of the numerical diffusion due to the use of large time step sizes without sub-iterations within the time step. Furthermore, the unsteady term also enhances the convergence of the employed iterative method (see Subsection 3.3.5 because of the increased diagonal contribution to the coefficient matrix.

Eqs. (1)-(3) are completed by appropriate boundary conditions (BCs) that can be written for a generic scalar field ϕ in a generic form as

$$\mathcal{B}(\phi) = \gamma \qquad \text{on } \Gamma, \tag{4}$$

where $\mathcal{B}$ is a linear differential operator, γ is a known function and $\Gamma = \partial\Omega$ is the boundary.

2.2. Solution procedure

At each time step n, the computation of velocity, pressure and temperature through Eqs. (1)-(3) is decoupled using a projection method for the pressure-velocity coupling [29]. A three-level Gear scheme is employed for the time discretization because of its improved stability properties over two-level schemes. A tentative velocity $\mathbf{u}^*$ is computed from the linearized momentum Eq. (2)

$$\frac{3\mathbf{u}^* - 4\mathbf{u}^{(n)} + \mathbf{u}^{(n-1)}}{2\Delta t} + \mathbf{u}^{(n)}\nabla\mathbf{u}^* = -\nabla p^{(n)} + \frac{1}{\mathrm{Re}}\nabla^2\mathbf{u}^*, \tag{5}$$

where $\Delta t = 1.0$ is the chosen nondimensional time step size, which corresponds to a dimensional time step size $\Delta t^* = H/U_0$ of the original, i.e., nondimensionalized, problem setting. $\mathbf{u}^*$ is then forced to satisfy the continuity equation (1) by means of an irrotational correction

$$\mathbf{u}^{(n+1)} = \mathbf{u}^* - \nabla\Phi, \tag{6}$$

leading to the following Poisson equation in the auxiliary variable Φ

$$\nabla^2\Phi = \nabla\cdot\mathbf{u}^*. \tag{7}$$

Homogeneous Neumann BCs for Φ are employed where Dirichlet BCs are imposed on $\mathbf{u}$, i.e., on $\Gamma_u \subseteq \Gamma$

$$\mathscr{B}(\Phi) = \frac{\partial\Phi}{\partial\mathbf{n}} = \nabla\Phi\cdot\mathbf{n} = 0 \qquad \text{on } \Gamma_u, \tag{8}$$

where $\mathbf{n}$ is the exterior normal to the boundary. Similarly, homogeneous Dirichlet BCs for Φ are employed where Neumann BCs are imposed on $\mathbf{u}$, i.e., on $\Gamma_p = \Gamma \setminus \Gamma_u$

$$\mathscr{B}(\Phi) = \Phi = 0 \qquad \text{on } \Gamma_p. \tag{9}$$

The pressure is then updated as

$$p^{(n+1)} = p^{(n)} + \frac{\Phi}{\Delta t} \tag{10}$$

and the temperature is computed from Eq. (3)

$$\frac{3T^{(n+1)} - 4T^{(n)} + T^{(n-1)}}{2\Delta t} + \mathbf{u}^{(n+1)}\nabla T^{(n+1)} = \frac{1}{\mathrm{Re}\ \mathrm{Pr}}\nabla^2 T^{(n+1)}. \tag{11}$$

The previous solution procedure represented by Eqs. (5)-(11) is performed once each time step, i.e., it is not iterated to convergence within each time step since only the steady-state solution is sought and there is no interest in the accurate solution of the time-dependent behaviour.

2.3. Auxiliary computations

In the case of non-isothermal flows the local Nusselt number Nu, in terms of nondimensional variables, is

$$\mathrm{Nu} = \left.\frac{\partial T}{\partial\mathbf{n}}\right|_{\Gamma} \tag{12}$$

and the mean Nusselt number $\overline{\mathrm{Nu}}$ is defined as

$$\overline{\mathrm{Nu}} = \frac{1}{L_h}\int_{\Gamma_h}\mathrm{Nu}\ \mathrm{d}\Gamma_h, \tag{13}$$

where Γ_h is the portion of the boundary where the heat transfer takes place and L_h is its total length.

3. Methodology

3.1. Non-intrusive Polynomial Chaos

The existing methods for uncertainty quantification can roughly be divided into two main categories: non-intrusive, or statistical, and intrusive, or non-statistical. Examples of non-intrusive approaches are Monte Carlo [30, 31], Stochastic Collocation [32, 33, 34], Chaos Collocation [6, 35, 36], metamodel-based methods [37, 14]. Stochastic Galerkin Finite Element Method [38] and Stochastic Spectral Method [2, 39, 40] are examples of intrusive approaches. The advantage of non-intrusive methods is to allow the use of existing deterministic solvers, whereas intrusive approaches need to modify the solver obtaining an efficient tool but limited to solve just a set of problems. So that non-intrusive methodologies have a simpler computational management.

Here a very brief description of the Non-intrusive Polynomial Chaos (PC) methodology used for the uncertainty quantification analysis is given in a steady-state formulation. More details can be found in [9, 15, 41].

Let $(\Theta, \mathcal{F}, \mathcal{P})$ be a probability space. Here Θ is the sample space, $\mathcal{F} \subset 2^{\Theta}$ its σ-algebra of events and $\mathcal{P}$ the associated probability measure. Given that the probability space can be described by a finite number n of independent random variables $\xi_1(\theta), \xi_2(\theta), \ldots, \xi_n(\theta) : \Theta \to \Re$ where θ represents an element of the sample space Θ, let us consider the following stochastic differential problem

$$\mathcal{L}(\mathbf{x}, \theta; \phi) = f(\mathbf{x}, \theta) \qquad \text{in} \quad \Omega(\theta), \tag{14}$$

$$\mathcal{B}(\mathbf{x}, \theta; \phi) = \gamma(\mathbf{x}, \theta) \qquad \text{on}\ \partial\Omega(\theta), \tag{15}$$

where $\mathbf{x}$ denotes the position, $\mathcal{L}$ is a differential operator which contains space differentiation and can be nonlinear, $f(\mathbf{x}, \theta)$ is the source term, Eq. (15) represents a stochastic boundary condition and $\phi := \phi(\mathbf{x}; \theta) : \Omega \times \Theta \to \Re$ is the solution. The randomness θ can enter the problem through $\mathcal{L}$ or f, through the boundary condition, i.e., through $\mathcal{B}$, γ or $\partial\Omega(\theta)$, or some combination.

The random solution ϕ can be expanded by the following Polynomial Chaos (PC) expansion

$$\phi(\mathbf{x}, \theta) = \sum_{i=1}^{N_P} \phi_i(\mathbf{x}) \psi_i\left(\boldsymbol{\xi}(\theta)\right), \tag{16}$$

where ψ_i are multivariate polynomials and $\boldsymbol{\xi}(\theta) = (\xi_1(\theta), \xi_2(\theta), \ldots, \xi_n(\theta))$ is the n-dimensional vector of random variables. The optimal set of expansion polynomials forms a complete orthogonal basis in $L_2(\Theta, \mathcal{F}, \mathcal{P})$ with orthogonality relation $\left\langle \psi_i, \psi_j \right\rangle = \left\langle \psi_i^2 \right\rangle \delta_{ij}$ where δ_{ij} is the Kronecker delta and $\langle \cdot, \cdot \rangle$ is the ensemble average $\left\langle \psi_i, \psi_j \right\rangle = \int_{\Theta} \psi_i\left(\boldsymbol{\xi}(\theta)\right) \psi_j\left(\boldsymbol{\xi}(\theta)\right)\, \mathrm{d}\mathcal{P}(\theta)$, i.e., ψ_i are orthogonal relative to the joint probability density function of $\boldsymbol{\xi}$.

A linear regression approach, also known as point collocation or chaos collocation, is employed to compute the coefficients (or modes) of the PC expansion, i.e., the functions $\phi_i(\mathbf{x})$, that is

$$\sum_{i=1}^{N_P} \phi_i\left(\mathbf{x}\right) \psi_i\left(\boldsymbol{\xi}(\theta_j)\right) = \phi\left(\mathbf{x}, \theta_j\right), \qquad j = 1, \ldots, M, \tag{17}$$

is solved for the N_P modes $\phi_i(\mathbf{x})$ that match the set of response values $\phi\left(\mathbf{x}, \theta_j\right)$ at M distinct samples θ_j. The set of response values is typically obtained by performing a random over-sampling of Θ. If a selected subset of Gaussian quadrature points is employed rather than a random over-sampling, the linear regression approach is referred as the Probabilistic Collocation Method, which provides more optimal collocation locations and preserves interpolation properties.

Known the coefficients of the PC expansion (16), the moments of the solution ϕ can be computed, so that the expected value and the variance are given by, respectively

$$\mu(\mathbf{x}; \phi) = \phi_1(\mathbf{x}), \tag{18}$$

$$\sigma^2(\mathbf{x}; \phi) = \sum_{i=2}^{N_P} \phi_i^2(\mathbf{x}) \left\langle \psi_i^2 \right\rangle, \tag{19}$$

where $\phi_1(\mathbf{x})$ denotes the mode associated to the constant polynomial ψ_1.

In this work normal distributions are considered only, therefore Hermite polynomials are employed in the PC expansion. In particular a tensor-product expansion is used, where the polynomial degrees are considered equal to P along each of the n dimensions of the probability space, leading to $N_P = (P+1)^n$ modes. The collocation points, i.e., the values $\xi_k(\theta_j)$, for $k = 1, \ldots, n$ and $j = 1, \ldots, M = N_P$, are the Gauss-Hermite quadrature points, that is the roots of the Hermite polynomial with degree $P+1$ along each of the n dimensions.

More efficient choices of collocation points have been proposed in literature [42, 43, 44, 45], for problems with high numbers of uncertain parameters. But the use of this particular methodology allows to compare the results with previous works [11, 46]. Moreover, in this paper we will consider problems with low dimensionality of uncertainty space, therefore no excessive computational effort is needed using the described method.

3.2. RBF-FD Meshless Method

The evaluation of the random process ϕ at the sample points θ_j can be calculated with a suitable deterministic solver. Most fluid dynamics solvers, both commercial and open-source, need a mesh/grid/tessellation of the computational domain in order to properly discretize the governing PDEs. It easy to understand that a solver which does not need such a mesh/grid/tessellation is a major advantage if we intend to analyze the effects of geometric uncertainties of the boundaries on the flow field. In this perspective the RBF-FD meshless method is employed and its basis are described as follows.

3.3. RBF-FD discretization

3.3.1. 2D node distributions

The 2D node distributions required by the RBF-FD meshless discretization have been obtained through the node generation algorithm proposed in [47, 20] which is composed by two distinct phases:

1. Quadtree node placing. Nodes are placed inside the domain Ω according to a prescribed spacing function $s(\mathbf{x})$ by using a quadtree space partitioning technique [48]. The quadtree technique is improved by using a dithering

correction [49] in order to reduce the nodal quantization error between the integer number of nodes that can be placed in any portion $\mathcal{P} \subseteq \Omega$ and the prescribed number $\int_{\mathcal{P}} 2s(\mathbf{x})^{-2}\ \mathrm{d}\mathcal{P}/\sqrt{3}$ which is non-integer in general. Without the dithering correction, the nodal quantization error can accumulate over the domain resulting in large portions with constant nodal spacing even if the prescribed spacing function $s(\mathbf{x})$ varies smoothly.

2. Node-repel refinement. The initial node distribution is then refined by means of an iterative tecnhique based on the mutual repulsion of nodes: each node $\mathbf{x}_i$ moves according to the radial repulsion forces of the $n = 12$ closest neighbouring nodes. The magnitude F of the nondimensional force exerted by node $\mathbf{x}_j$ on node $\mathbf{x}_i$ is chosen to be

$$F(r_{ji}) = (r_{ji}^2 + \beta^2)^{-2}, \tag{20}$$

where $r_{ji} = \|\mathbf{x}_i - \mathbf{x}_j\|/s(\mathbf{x}_j)$ is the normalized distance between the nodes and $\beta = 1/2$ is a limiting parameter. Note that the unsymmetrical formulation of r_{ji} is required in order to satisfy the prescribed spacing function $s(\mathbf{x})$ in the asymptotic limit of the iterative process. The dimensional displacement of node $\mathbf{x}_i$ at iteration k is then

$$\mathbf{x}_i^{(k+1)} - \mathbf{x}_i^{(k)} = \alpha s(\mathbf{x}_i) \sum_{j \in J(\mathbf{x}_i^{(k)})} F(r_{ji})\ \hat{\mathbf{e}}\left(\mathbf{x}_i^{(k)} - \mathbf{x}_j^{(k)}\right), \tag{21}$$

where $\alpha = 0.05$ is a nondimensional displacement factor, $\hat{\mathbf{e}}(\mathbf{y}) = \mathbf{y}/\|\mathbf{y}\|$ is the vector normalization operator for the radial direction and $J(\mathbf{x}_i)$ is the index set of the n nodes $\mathbf{x}_j$ closest to $\mathbf{x}_i$ according to the Euclidean norm $\|\cdot\| = \|\cdot\|_2$. A fixed boundary distribution of nodes matching $s(\mathbf{x})$ is employed during this phase. 100 refinement iterations are employed, which are typically enough to obtain very high quality node distributions.

The resulting distribution is a set of $N \approx \int_{\Omega} 2s(\mathbf{x})^{-2}\ \mathrm{d}\Omega/\sqrt{3}$ nodes $\mathbf{x}_i$ which are isotropically displaced over the domain Ω and over its boundary $\Gamma = \partial\Omega$ according to the prescribed spacing function $s(\mathbf{x})$.

3.3.2. Local RBF interpolation

A scalar field $\phi(\mathbf{x})$ is approximated near $\mathbf{x} \in \Omega$ by a local RBF interpolant $\tilde{\phi}(\mathbf{x})$, which is composed by a RBF expansion augmented with a polynomial [50]

$$\phi(\mathbf{x}) \approx \tilde{\phi}(\mathbf{x}) = \underbrace{\sum_{j=1}^{n} a_j \varphi\left(\|\mathbf{x} - \mathbf{x}_j\|\right)}_{\text{RBF expansion}} + \underbrace{\sum_{k=1}^{m} c_k g_k\left(\mathbf{x} - \bar{\mathbf{x}}\right)}_{\text{polynomial}}, \tag{22}$$

where the supporting nodes $\mathbf{x}_j$ are the n neighbouring nodes closest to $\mathbf{x}$, $\bar{\mathbf{x}}$ is their mean position, $\varphi(\|\cdot\|)$ are Radial Basis Functions and a_j are the corresponding expansion coefficients. The functions g_k form a complete 2D polynomial basis of degree q with $m = \binom{q+2}{q}$ terms and c_k are the corresponding coefficients. From another point of view, the expansion (22) can be viewed as a classic polynomial expansion, which accounts for the accuracy and the smoothness of the interpolant, augmented with a RBF expansion which alleviates the ill-posed problem of polynomial scattered data interpolation in more than one dimension, allowing well-conditioned interpolants over arbitrarily scattered nodes if certain conditions are met [50, 18, 19].

The multiquadric RBF [51, 52, 17] has been chosen since it is strictly conditionally positive definite of order one, allowing a well-posed interpolation when a polynomial augmentation of degree $q \geq 0$ is employed (this holds also without polynomial augmentation [50]), and it is proven to be one of the best choices for scattered data interpolation [53, 54]

$$\varphi(r) = \sqrt{1 + (\varepsilon r)^2}, \tag{23}$$

where the shape factor ε has been rescaled with the local spacing s as $\varepsilon = 0.35/s(\bar{\mathbf{x}})$, i.e., stationary interpolation [50]. Despite the fact that increasingly flat RBFs (i.e., $\varepsilon \to 0$) allow better accuracy [55], the previous choice of stationary interpolation is due to stability requirements in the solution of the discretized equations/time integration.

The interpolant (22) must match the unknown field ϕ at the $n_I \leq n$ supporting nodes $\mathbf{x}_i$ which do not lie on the boundary Γ

$$\phi\left(\mathbf{x}_i\right) = \phi_i = \sum_{j=1}^{n} a_j \varphi\left(\|\mathbf{x}_i - \mathbf{x}_j\|\right) + \sum_{k=1}^{m} c_k g_k\left(\mathbf{x}_i - \bar{\mathbf{x}}\right), \qquad i = 1, \ldots, n_I. \tag{24}$$

If any of the supporting nodes lie on the boundary Γ, the interpolant (22) is enforced to satisfy the corresponding boundary condition on these $n_B = n - n_I$ boundary nodes $\hat{\mathbf{x}}_b$

$$\mathcal{B}\left(\tilde{\phi}\right)\Big|_{\hat{\mathbf{x}}_b} = \sum_{j=1}^{n} a_j \Psi\left(\hat{\mathbf{x}}_b\right) + \sum_{k=1}^{m} c_k G_k\left(\hat{\mathbf{x}}_b\right) = \gamma\left(\hat{\mathbf{x}}_b\right) = \gamma_b, \qquad b = 1, \ldots, n_B, \tag{25}$$

where $\Psi_j(\mathbf{x}) = \mathcal{B}\left(\varphi(\|\mathbf{x} - \mathbf{x}_j\|)\right)$ and $G_k(\mathbf{x}) = \mathcal{B}\left(g_k(\mathbf{x} - \bar{\mathbf{x}})\right)$.

In order to guarantee the polynomial reproduction, i.e., the exactness of interpolant (22) for polynomials up to degree q, the following conditions are required

$$\sum_{j=1}^{n} a_j g_k\left(\mathbf{x}_j - \bar{\mathbf{x}}\right) = 0, \qquad k = 1, \ldots, m. \tag{26}$$

By collecting the $n_I + n_B + m = n + m$ conditions expressed by Eqs. (24)-(26), the following local linear system is obtained

$$\left[\begin{array}{ccc|ccc}
\varphi(\|\mathbf{x}_1 - \mathbf{x}_1\|) & \cdots & \varphi(\|\mathbf{x}_1 - \mathbf{x}_n\|) & g_1(\mathbf{x}_1 - \bar{\mathbf{x}}) & \cdots & g_m(\mathbf{x}_1 - \bar{\mathbf{x}}) \\
\vdots & \ddots & \vdots & \vdots & \ddots & \vdots \\
\varphi(\|\mathbf{x}_{n_I} - \mathbf{x}_1\|) & \cdots & \varphi(\|\mathbf{x}_{n_I} - \mathbf{x}_n\|) & g_1(\mathbf{x}_{n_I} - \bar{\mathbf{x}}) & \cdots & g_m(\mathbf{x}_{n_I} - \bar{\mathbf{x}}) \\
\hline
\Psi_1(\hat{\mathbf{x}}_1) & \cdots & \Psi_n(\hat{\mathbf{x}}_1) & G_1(\hat{\mathbf{x}}_1) & \cdots & G_m(\hat{\mathbf{x}}_1) \\
\vdots & \ddots & \vdots & \vdots & \ddots & \vdots \\
\Psi_1(\hat{\mathbf{x}}_{n_B}) & \cdots & \Psi_n(\hat{\mathbf{x}}_{n_B}) & G_1(\hat{\mathbf{x}}_{n_B}) & \cdots & G_m(\hat{\mathbf{x}}_{n_B}) \\
\hline
g_1(\mathbf{x}_1) & \cdots & g_1(\mathbf{x}_n) & 0 & \cdots & 0 \\
\vdots & \ddots & \vdots & \vdots & \ddots & \vdots \\
g_m(\mathbf{x}_1) & \cdots & g_m(\mathbf{x}_n) & 0 & \cdots & 0
\end{array}\right]
\begin{Bmatrix} a_1 \\ \vdots \\ a_n \\ c_1 \\ \vdots \\ c_m \end{Bmatrix}
=
\begin{Bmatrix} \phi_1 \\ \vdots \\ \phi_{n_I} \\ \gamma_1 \\ \vdots \\ \gamma_{n_B} \\ 0 \\ \vdots \\ 0 \end{Bmatrix}. \tag{27}$$

The compact notation for linear system (27) is

$$\mathbf{B}\begin{pmatrix}\mathbf{a}\\ \mathbf{c}\end{pmatrix}=\begin{pmatrix}\boldsymbol{\phi}\\ \boldsymbol{\gamma}\\ \mathbf{0}\end{pmatrix},\tag{28}$$

where $\mathbf{B}\in\Re^{(n+m)\times(n+m)}$ is the nonsingular interpolation matrix, $\mathbf{a}=(a_j)\in\Re^n$ is the column vector of RBF expansion coefficients, $\mathbf{c}=(c_k)\in\Re^m$ is the column vector of polynomial coefficients, $\boldsymbol{\phi}=(\phi_i)\in\Re^{n_I}$ is the column vector of nodal values of ϕ at the n_I internal nodes, $\boldsymbol{\gamma}=(\gamma_b)\in\Re^{n_B}$ is the column vector of BCs known term γ at the n_B boundary nodes and $\mathbf{0}\in\Re^m$ is a column vector of zeros.

By using this notation and by solving Eq. (28) for the expansion coefficients **a** and **c**, the RBF interpolant (22) can be written as

$$\tilde{\phi}(\mathbf{x})=\begin{pmatrix}\boldsymbol{\varphi}(\mathbf{x})\\ \mathbf{g}(\mathbf{x})\end{pmatrix}^T\begin{pmatrix}\mathbf{a}\\ \mathbf{c}\end{pmatrix}=\begin{pmatrix}\boldsymbol{\varphi}(\mathbf{x})\\ \mathbf{g}(\mathbf{x})\end{pmatrix}^T\mathbf{B}^{-1}\begin{pmatrix}\boldsymbol{\phi}\\ \boldsymbol{\gamma}\\ \mathbf{0}\end{pmatrix},\tag{29}$$

where $\boldsymbol{\varphi}(\mathbf{x})=\left(\varphi(\|\mathbf{x}-\mathbf{x}_j\|)\right)\in\Re^n$ is the column vector of RBFs for the n supporting nodes and $\mathbf{g}(\mathbf{x})=(g_k(\mathbf{x}-\bar{\mathbf{x}}))\in\Re^m$ is the column vector of polynomial basis functions.

3.3.3. RBF-FD collocation

Let us consider a linear PDE in the unknown field $\phi(\mathbf{x})$

$$\mathcal{L}(\phi(\mathbf{x}))=f(\mathbf{x}),\tag{30}$$

where $\mathcal{L}$ is a linear differential operator and f is a known function, and let us define the residual of PDE (30) as $\mathcal{R}(\phi(\mathbf{x})):=\mathcal{L}(\phi(\mathbf{x}))-f(\mathbf{x})$. A collocation approach is then employed to obtain the required set of discrete RBF-FD equations by setting the residual of the RBF interpolant $\tilde{\phi}(\mathbf{x})$ equal to zero at each of the N_I nodes $\mathbf{x}_i$ which do not lie on the boundary Γ

$$\mathcal{R}\left(\tilde{\phi}(\mathbf{x})\right)=0,\qquad \mathbf{x}=\mathbf{x}_i,\ i=1,\dots,N_I.\tag{31}$$

By taking the RBF interpolant in the form of Eq. (29), Eq. (31) becomes

$$\mathcal{R}\left(\tilde{\phi}(\mathbf{x})\right)=\mathcal{L}\left(\tilde{\phi}(\mathbf{x})\right)-f(\mathbf{x})=\underbrace{\begin{pmatrix}\mathcal{L}(\boldsymbol{\varphi}(\mathbf{x}))\\ \mathcal{L}(\mathbf{g}(\mathbf{x}))\end{pmatrix}^T\mathbf{B}^{-1}}_{\mathbf{w}^T(\mathbf{x})}\begin{pmatrix}\boldsymbol{\phi}\\ \boldsymbol{\gamma}\\ \mathbf{0}\end{pmatrix}-f(\mathbf{x})=0,\qquad \mathbf{x}=\mathbf{x}_i,\ i=1,\dots,N_I,\tag{32}$$

where the operator $\mathcal{L}$ is applied to the RBFs vector $\boldsymbol{\varphi}(\mathbf{x})$ and to the polynomial basis vector $\mathbf{g}(\mathbf{x})$ because of the linearity of $\mathcal{L}$. Eq. (32) shows that the stencil coefficients, i.e., the first n_I components of vector $\mathbf{w}(\mathbf{x}_i)$, can be computed by solving the following linear system

$$\mathbf{B}^T \mathbf{w}(\mathbf{x}_i) = \begin{pmatrix} \mathcal{L}(\boldsymbol{\varphi}(\mathbf{x})) \\ \mathcal{L}(\mathbf{g}(\mathbf{x})) \end{pmatrix}_{\mathbf{x}=\mathbf{x}_i}, \tag{33}$$

which is accurately solved by means of a LDL^T factorization of the symmetric part of $\mathbf{B}^T$ with a Schur complement [56] accounting for the nonsymmetric part of $\mathbf{B}^T$ due to possible boundary nodes where non-Dirichlet BCs are imposed, i.e., where $\mathscr{B}(\phi) \neq \alpha\phi$. A sparse $N_I \times N_I$ linear system representing the RBF-FD discretization of the linear PDE (30) over the domain Ω is then obtained from the N_I equations (32), each of which requires the solution of the local system (33).

3.3.4. Stabilization

Eqs. (5), (7) and (11) are discretized with the same RBF-FD scheme previously presented in Section 3.3. It is known that a naive discretization of these equations can lead to spurious solutions/instabilities due to two causes: the pressure-velocity coupling, i.e., the pressure gradient ∇p in Eq. (2), and the advective term $\mathbf{u} \cdot \nabla$ in Eqs. (2)-(3), both involving first order space derivatives. The former comes in the form of spurious pressure modes and can be overcome by using well-known remedies, e.g., staggered grids in the FDM and FVM [57], unequal order discretization schemes for pressure and velocity in the FEM [58, 59], Rhie-Chow interpolation on co-located grids [60]. The latter comes in the form of spurious velocity modes and is commonly overcome by means of upwinding techniques [61].

In the context of the RBF-FD method it is desirable to have a common discretization scheme defined on a common node distribution for the entire set of variables, e.g., $\mathbf{u}$, p and T, while upwind techniques, although employed [62, 63, 64], tend to be avoided in favour of other techniques [65], expecially when dealing with high-order, accurate RBF-FD discretizations.

A powerful and yet accurate technique which can be employed to overcome both types of instabilities is hyperviscosity [66, 16], which consists of adding enough amount δ of artificial diffusivity to the transport Eqs. (2)-(3), in the form of an iterated laplacian Δ^k with $k > 1$, in order to stabilize the discretization, i.e., avoiding the presence of eigenmodes with unstable eigenvalues. The advantage of hyperviscosity over traditional stabilization methods is the possibility to select the exponent k in order to ensure the artificial diffusivity to vanish faster than the discretization error of the RBF-FD method itself under node refining, i.e., reducing the nodal spacing s.

Consider a harmonic component f with spatial frequency $\boldsymbol{\omega}$

$$f = e^{j\boldsymbol{\omega}\cdot\mathbf{x}/s - \lambda t}, \tag{34}$$

the resulting temporal decay rate λ due to the hyperviscosity smoothing $\delta\Delta^k$ is [20]

$$\lambda = \delta \frac{\|\boldsymbol{\omega}\|_2^{2k}}{s^{2k}} (-1)^{k+1}, \tag{35}$$

which shows that spurious components with wave-length comparable to the nodal spacing s, i.e., $\|\boldsymbol{\omega}\|_2 \approx 1$, sustain large damping while physical informations, i.e., $\|\boldsymbol{\omega}\|_2 \ll 1$, sustain small damping. Since the decay rate λ must be positive and independent upon the spacing s for a given $\boldsymbol{\omega}$, we obtain

$$\delta = \bar{\delta} s^{2k} (-1)^{k+1}, \tag{36}$$

where $\bar{\delta} > 0$ is the specific amount of hyperviscosity. Eq. (36) shows that the amount δ of artificial hyperviscosity introduced in the equations vanishes with order $2k$ under node refining. Therefore the exponent k should be chosen to satisfy $2k \geq l$ in order to obtain a consistent discretization, where l is the order of accuracy of the RBF-FD discretization. Since the order of accuracy of the RBF-FD discretizations employed in this work never exceeds $l = 6$, an hyperviscosity exponent $k = 3$ is always employed.

The pressure, which is governed by Poisson Eq. (7) which is not a transport equation, can anyway be stabilized through an explicit hyperviscosity stabilization: at each time step the pressure $p^{(n+1)}$, obtained from Eq. (10), is corrected to obtain $\tilde{p}^{(n+1)}$ as follows

$$\tilde{p}^{(n+1)} = \left(I + \bar{\delta}_p s^{2k} (-1)^{k+1} \Delta^k \right) p^{(n+1)}, \tag{37}$$

where $\bar{\delta}_p > 0$ is the specific amount of explicit hyperviscosity for the pressure. In Eq. (37) the BCs for the explicit hyperviscosity operator Δ^k are the same for the Poisson Eq. (7), i.e., Eqs. (8)-(9).

The specific amounts of hyperviscosity $\bar{\delta}$, which can differ for momentum and energy Eqs. (2)-(3), and $\bar{\delta}_p$ have been found by trial and error on the base of very short test runs, as suggested in [66].

3.3.5. Solution of the discretized equations

The discretized equations resulting from the RBF-FD discretization consist of two sparse linear systems for the two-dimensional components of the velocity $\mathbf{u} = (u, v)$, Eq. (5), one sparse linear system for the auxiliary variable Φ, Eq. (7), and one sparse linear system for the temperature, Eq. (11); each of the previous linear systems need to be solved at each time step. A BiCGSTAB iterative solver [67] with an incomplete *LU* factorization (ILU) as preconditioner [68] are employed for the solution of the discretized transport equations of velocity and temperature, Eq. (5) and Eq. (11), using a relative tolerance $tol = 10^{-9}$ on residuals. The threshold value for ILU is set to $thr = 0.005$ and the factorization is performed when the required number of BiCGSTAB iterations exceeds 75% of the number of iterations required immediately after the previous factorization. The discretized Poisson Eq. (7) is solved through a *LU* decomposition which can be performed once at the beginning of each simulation.

The steady-state convergence is declared when

$$\mathrm{NRMSE}\left(\mathbf{u}^{(n+1)}, \mathbf{u}^{(n)}\right) < 10^{-8}\mathrm{Re}\Delta t, \quad \mathrm{NRMSE}\left(T^{(n+1)}, T^{(n)}\right) < 10^{-8}\mathrm{RePr}\Delta t. \tag{38}$$

NRMSE is the normalized root mean square error

$$\mathrm{NRMSE}(\mathbf{q}, \hat{\mathbf{q}}) = \sqrt{\frac{1}{A(\hat{\Omega})} \int_{\hat{\Omega}} \frac{\|\mathbf{q} - \hat{\mathbf{q}}\|_2^2}{\max_{\hat{\Omega}} \left(\|\hat{\mathbf{q}}\|_2^2 \right)} \, \mathrm{d}\hat{\Omega}} \approx \sqrt{\left(\sum_{i \in \hat{I}} s^2(\mathbf{x}_i) \right)^{-1} \sum_{i \in \hat{I}} \frac{\|\mathbf{q}(\mathbf{x}_i) - \hat{\mathbf{q}}(\mathbf{x}_i)\|_2^2}{\max_{\hat{\Omega}} \left(\|\hat{\mathbf{q}}(\mathbf{x}_i)\|_2^2 \right)} s^2(\mathbf{x}_i)}, \tag{39}$$

where $A(\hat{\Omega})$ is the area of $\hat{\Omega}$, $\hat{\mathbf{q}}$ is a reference field, $\hat{\Omega}$ is a reference domain and $\hat{I}$ is the index set of nodes $\mathbf{x}_i$ belonging to $\hat{\Omega}$. The reference domain coincides with the actual domain, i.e., $\hat{\Omega} = \Omega$, unless otherwise specified.

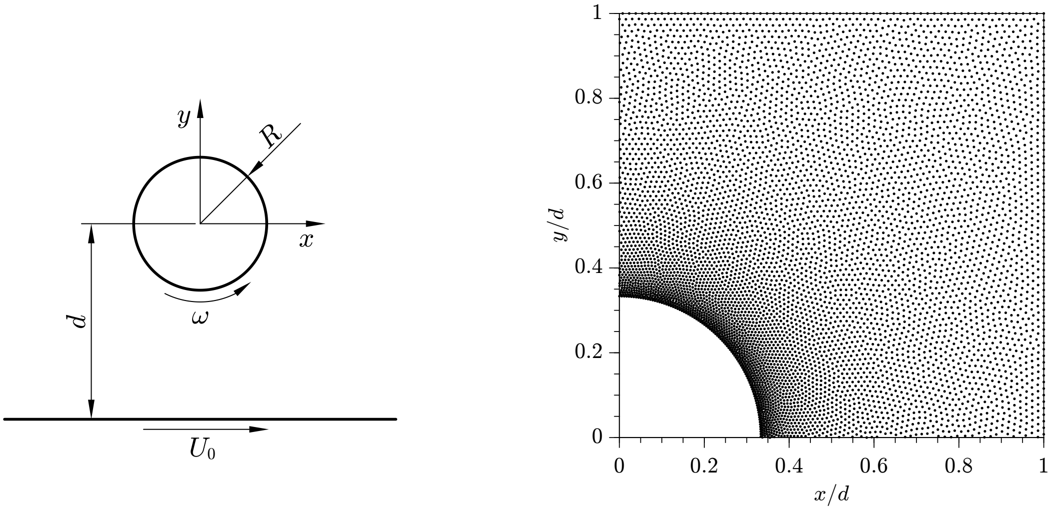

(a) (b)

Fig. 1: Sketch of the flow past a spinning cylinder near a moving wall (a). Particular of the node distribution with $N = 54,327$ nodes (b).

4. Numerical results

4.1. Wannier Flow

4.1.1. Geometry and boundary conditions

A Wannier flow, i.e., a two-dimensional, isothermal Stokes flow past a rotating circular cylinder near a moving wall, is considered. The governing equations for Stokes flow are obtained from Eqs. (1)-(2) by neglecting the unsteady and the advective terms in the momentum equation which becomes

$$\mathrm{Re}\nabla p = \nabla^2 \mathbf{u}, \tag{40}$$

where Re = 1 is considered for simplicity since it acts as a multiplicative factor for the pressure. Dirichlet BCs are employed for the velocity along the entire boundary.

The Wannier flow is a particularly meaningful test case since an explicit analytical solution for the velocity $\mathbf{u} = (u, v)$ is available in terms of d, R, U_0 and ω, where the distance from the cylinder center to the wall, d, and the cylinder radius, R, are geometrical quantities (see Fig. 1(a)), as reported in Appendix A.

The numerical domain is

$$\Omega = \left\{ \mathbf{x} \in \Re^2 \mid \mathbf{x} \in [-d, d]^2, ||\mathbf{x}||_2 \geq R \right\}. \tag{41}$$

In order to avoid spurious pressure gradients at the boundary due to the employed projection scheme [69], the initial pressure field at $t = 0$ is computed numerically by considering the divergence of Eq. (40)

$$\nabla^2 p = 0, \tag{42}$$

where the continuity Eq. (1) is invoked. Neumann BCs are imposed by taking the normal component of Eq. (40)

$$\frac{\partial p}{\partial \mathbf{n}} = \mathbf{n} \cdot \nabla^2 \mathbf{u}, \tag{43}$$

where the RHS is explicitly computed from the analytical solution reported in Appendix A.

4.1.2. Spacing function

The employed spacing function for node generation is

$$s(\mathbf{x}) = s_{\min} + (s_{\max} - s_{\min}) \frac{\arctan(a_W z_W)}{\arctan(a_W)}, \tag{44}$$

where $s_{\min}$ and $s_{\max} = 3s_{\min}$ are the minimum and maximum spacing, respectively, $a_W = 5$ and $z_W = \left(\sqrt{x^2+y^2} - R\right)/d$ is the nondimensional distance from the cylinder wall. An example of node distribution with $N = 54,327$ nodes for a geometry with $d/R = 3$ is depicted in Fig. 1(b), where it can be observed an increasing node density, i.e., number of nodes per unit area, towards the cylinder wall according to the prescribed spacing function.

4.1.3. Validation of the deterministic model

In order to validate the deterministic RBF-FD solver, different convergence tests are carried out by increasing the total number of nodes from $N \approx 4,000$ to $N \approx 200,000$ to assess the convergence properties of the numerical model. The chosen parameters for the Wannier flow are $d = 0.75$, $R = 0.25$, $U_0 = 1.0$. By considering the analytical solution reported in Appendix A as reference, the resulting convergence curves for the NRMSE of the velocity are depicted in Fig. 2(a) for four different RBF-FD schemes with polynomial order $q = 2$, 3, 4 and 5 for which the corresponding number of supporting nodes is chosen to be $n = 20$, 25, 30 and 40 [20], respectively. The resulting order of accuracy varies from $l = 1.6$ for a polynomial degree $q = 2$ to $l = 4.8$ for a polynomial degree $q = 5$, with an unexpectedly high order $l = 4.8$ for a polynomial degree $q = 4$. Based on the previous observations, a RBF-FD scheme with polynomial degree $q = 4$ and $n = 30$ supporting nodes is chosen for the following calculations.

4.1.4. Results of the stochastic model

The uncertain parameters are chosen to be the distance d from the cylinder center to the wall, and the cylinder radius R, both having a normal distribution with a standard deviation equal to 5% of the corresponding mean value, i.e.,

$$d \sim \mathcal{N}\left(d_0, (0.05 d_0)^2\right), \qquad R \sim \mathcal{N}\left(R_0, (0.05 R_0)^2\right), \tag{45}$$

where $d_0 = 0.25$ and $R_0 = 0.75$. For each sample of the uncertain parameters required by the PC procedure, a different node distribution for the RBF-FD discretization is actually generated over the corresponding geometry.

Different convergence tests for the statistical moments, i.e., mean μ and standard deviation σ of the cartesian components (u, v) of the velocity, are carried out by increasing the polynomial order of the PC expansion from $P = 1$ to $P = 6$, while the reference statistical moments for the NRMSE are obtained for $P = 8$ and using the analytical solution reported in Appendix A for the $N_P = (P+1)^2$ deterministic response evaluations. The domain of integration

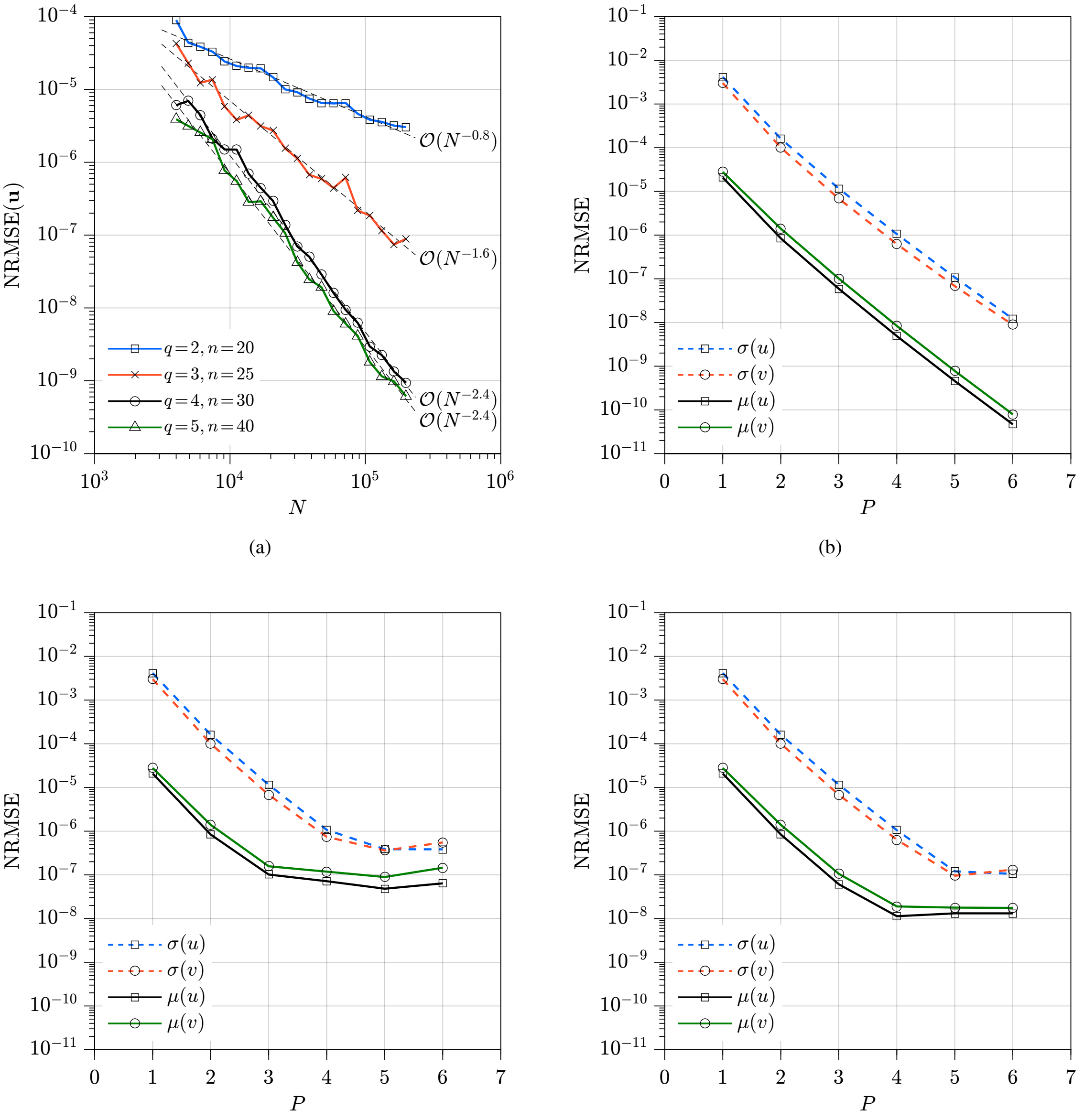

(a) (b)

(c) (d)

Fig. 2: Deterministic Wannier flow solved by RBF-FD: normalized RMS errors vs. number of nodes N (a). Stochastic Wannier flow solved by PC, normalized RMS errors vs. PC order P: analytical solution (b), RBF-FD solution with $N = 25,636$ nodes (c), RBF-FD solution with $N = 54,327$ nodes (d).

$\hat{\Omega}$ for the calculation of NRMSE in Eq. (39) is given by the intersection of each of the different deterministic domains required by the PC procedure, i.e., the points where the required deterministic solutions are simultaneously available.

The convergence curves for the NRMSE of the statistical moments are depicted in Fig. 2(b) when using the analytical solution for the evaluation of the deterministic responses. The observation of these curves reveal a clear exponential convergence for both moments of both u and v when increasing P, confirming the spectral accuracy of the PC method.

The NRMSE convergence curves depicted in Fig. 2(c) and 2(d) are obtained by using a RBF-FD discretization

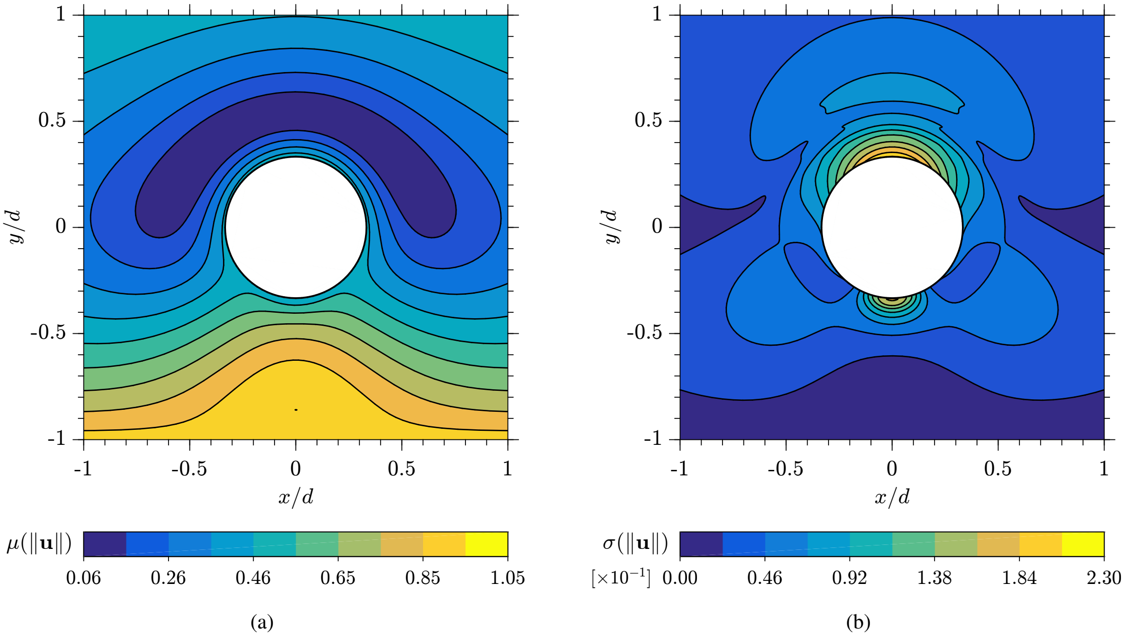

(a) (b)

Fig. 3: Stochastic Wannier flow: velocity mean contours (a) and velocity standard deviation contours (b).

with $N \approx 25,000$ and $N \approx 50,000$ nodes, respectively, for the evaluation of the deterministic responses. The chosen RBF-FD scheme employs polynomial degree $q = 4$ and $n = 30$ supporting nodes, while a new node distribution is generated for each required deterministic response, i.e., for each couple of geometrical parameters (d, R). The observation of the convergence curves for both cases suggests that the exponential convergence holds as long as the RBF-FD discretization error is lower than the PC error, as expected. Indeed, the exponential convergence for the case with $N \approx 25,000$ nodes, Fig. 2(c), holds up to $P = 3$ for μ and up to $P = 4$ for σ, namely where the NRMSE of the considered moment is within the same order of magnitude of the NRMSE of the deterministic solver, Fig. 2(a), i.e., NRMSE $\approx 10^{-7}$. Similarly, the exponential convergence for the case with $N \approx 50,000$ nodes, Fig. 2(d), holds up to $P = 4$ for μ and up to $P = 5$ for σ, again where the NRMSE of the considered moment falls within the same order of magnitude of the NRMSE of the deterministic solver, i.e., NRMSE $\approx 10^{-8}$. Contour plots of mean and standard deviation of velocity magnitude $\|\mathbf{u}\|_2$, obtained with PC order $P = 6$ and using the analytical solution, are depicted in Fig. 3.

4.2. Backward-facing step

4.2.1. Geometry and boundary conditions

A two-dimensional, isothermal steady flow over a backward facing step at Re = 600 and Re = 800 is considered. It is a standard test case problem being addressed by numerous authors using a variety of numerical and experimental methods [70, 71, 72, 73, 11]. The geometry of the problem and a schematic illustration of the flow are shown in Fig. 4. The fluid enters the channel at the left inlet with a prescribed parabolic profile with average velocity U_0 and flows past a step of height h, with downstream channel height $H = 2h$. After the flow separates at the step, the flow reattaches to the lower wall at $x = x_1$. At the upper wall the flow separates at $x = x_2$ and reattaches at $x = x_3$.

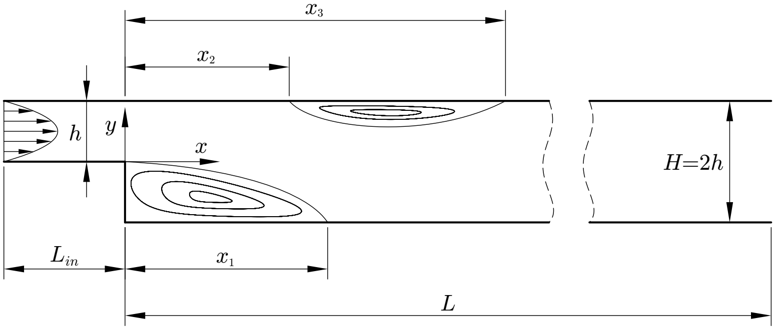

Fig. 4: Flow over a backward-facing step: schematic illustration of geometry and flow field.

Completely developed flow BCs are employed at the channel outlet, i.e., $\partial\mathbf{u}/\partial x = \mathbf{0}$ and $p = 0$ are imposed. The length of the upstream section of the channel is $L_{in} = 10h/3$ while the downstream section length is $L = 60h$, which are the dimensions employed in [11]

4.2.2. Spacing function

The spacing function for node generation is obtained by combining three contributions for the required node density: an increase at the walls for a better resolution of the wall gradients, a localized increase at the step corner for a better resolution of the corner singularity, and a gradual decrease towards the channel outlet to reduce the number of nodes where the flow is almost completely developed. The first contribution, i.e., the increased node density at the walls, is expressed by factor s_1

$$s_1(\mathbf{x}) = s_{\min} + (s_{\max} - s_{\min})\frac{\arctan(a_W z_W)}{\arctan(a_W)}, \tag{46}$$

where $s_{\min}$ and $s_{\max} = 4s_{\min}$ are the minimum and maximum reference spacing, respectively, $a_W = 3$ and $z_W = d_w/h$ where z_W and d_W are the nondimensional and dimensional distances from the nearest wall, respectively. The second contribution, i.e., the increased node density at the step corner, is expressed by factor s_2

$$s_2(\mathbf{x}) = k_S + (1 - k_S)\frac{2}{\pi}\arctan(a_S z_S), \tag{47}$$

where $k_S = 40$, $a_S = 5$ and $z_S = d_S/h$ where z_S and $d_S = \|\mathbf{x} - \mathbf{x}_S\|_2$ are the nondimensional and dimensional distances from the step corner, respectively. The thirs contribution, i.e., the reduced node density towards the outlet, is expressed by factor s_3

$$s_3(\mathbf{x}) = 1 + k_O\frac{x}{L}, \tag{48}$$

where $k_O = 0.75$. The spacing function is then obtained by the product of the previous factors

$$s(\mathbf{x}) = s_1(\mathbf{x})s_2(\mathbf{x})s_3(\mathbf{x}). \tag{49}$$

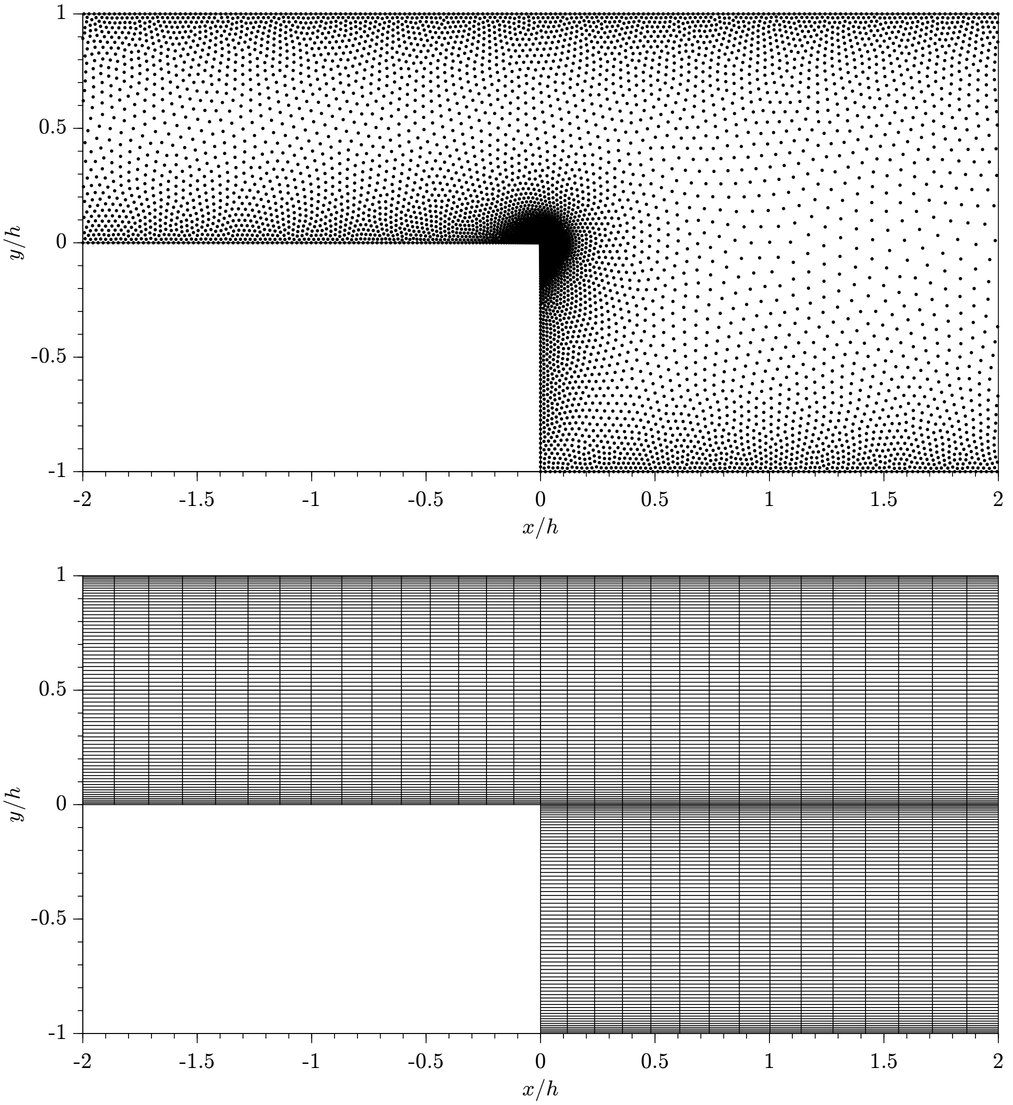

Fig. 5: Flow over a backward-facing step: particular of the node distribution with $N = 45,800$ nodes (top), particular of the OpenFOAM mesh with approximatively $40,000$ cells.

An example of node distribution with $N = 53,961$ nodes is depicted in Fig. 5, where it can be observed the prescribed increase in node density at the walls and at the step corner, according to the prescribed spacing function.

Similarly to the previous test case, polynomial degree $q = 4$ and $n = 30$ supporting nodes are always employed for the RBF-FD discretization.

4.2.3. Validation of the deterministic model

The RBF-FD solver is validated by considering the case Re = 800. A convergence test is carried out by increasing the total number of nodes from $N \approx 20,000$ to $N \approx 200,000$. By considering a computed solution with $N \approx 350,000$ as reference, the resulting convergence curves for the NRMSE of the velocity components (u, v) and pressure p are depicted in Fig. 6(a), where it can be observed that the resulting order of accuracy is $l = 3.2$ for each of the considered

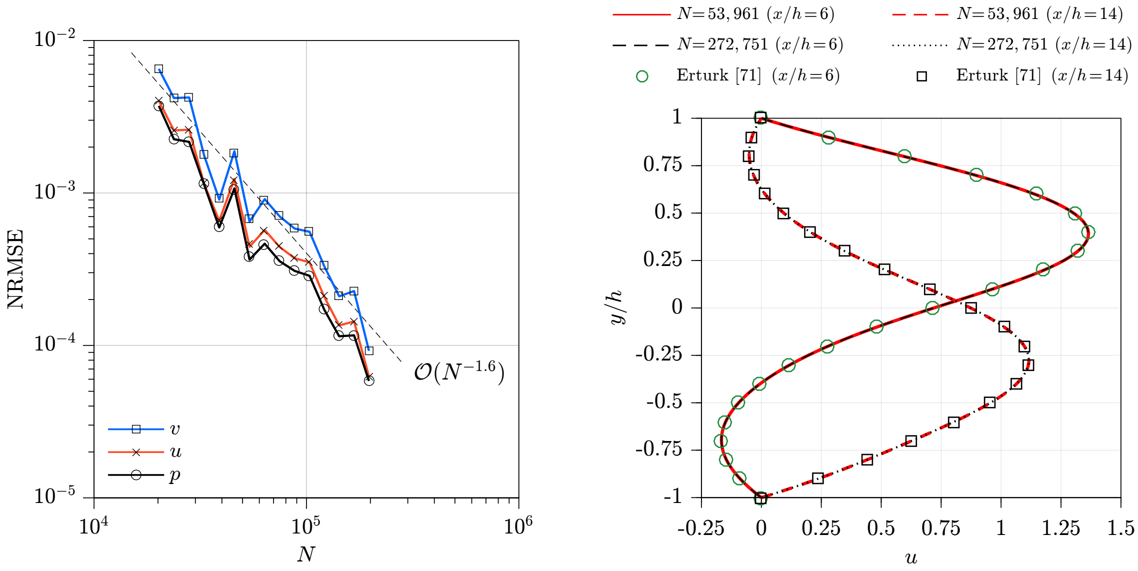

(a) (b)

Fig. 6: Deterministic flow over a backward-facing step at Re=800 solved by RBF-FD: normalized RMS errors vs. number of nodes N (left), comparison of u-velocity profiles (right).

Table 1: Normalized locations of detachment and reattachment of the deterministic flow over a backward-facing step at Re=800.

N	x_1/h	x_2/h	x_3/h
20,186	11.614	9.471	20.263
23,773	11.671	9.488	20.319
28,051	11.674	9.457	20.320
33,002	11.726	9.496	20.358
38,854	11.747	9.496	20.418
45,800	11.734	9.454	20.455
53,961	11.760	9.486	20.427
63,600	11.760	9.447	20.447
74,815	11.767	9.448	20.472
88,058	11.770	9.454	20.460
103,443	11.772	9.442	20.473
121,271	11.782	9.428	20.483
142,596	11.785	9.430	20.493
167,559	11.786	9.428	20.505
196,903	11.792	9.418	20.507
231,754	11.796	9.412	20.511
272,751	11.795	9.412	20.517
∞ (extrap.)	11.799	9.405	20.523
Erturk [71]	11.834	9.476	20.553

flow variables.

The convergence of the normalized locations of detachment and reattachment of the flow is reported in Table 1, where the extrapolations are obtained by least squares fitting of the curve $c_1 + c_2 N^{-l/2}$, $l = 3.2$. Reference results of Erturk [71] are also reported in Table 1, highlighting an excellent agreement for the computed values of x_1, x_2 and x_3 with less than 1% differences.

A comparison between the u-velocity profiles for two computed solutions with $N = 53,961$ and $N = 272,751$ nodes is depicted in Fig. 6(b), where the profiles computed in [71] are also shown. An excellent agreement with the reference results is again found, while the computed profiles for $N = 53,961$ and $N = 272,751$ nodes are almost identical to graphical accuracy. Indeed, the NRMSE of each flow variable is below 10^{-3} for $N = 53,961$ nodes, Fig. 6(a), and for this reason a meshless distribution with $N = 53,961$ nodes is chosen for each of the following computations over the backward-facing step.

4.2.4. Results of the stochastic model

Geometric tolerances of perpendicularity on the step are considered for Re=600. The position of the step corner $\mathbf{x}_S = (x_S, y_S)$ spans the uncertainty space, while the step walls remain straight but no longer aligned to the cartesian axes, with θ_H angular deviation of the horizontal step wall from the horizontal direction, i.e., x axis, and θ_V angular deviation of the vertical step wall from the vertical direction, i.e., y axis. By considering these deviations as uncertain parameters, the position of the step corner can be approximated by

$$\mathbf{x}_S = (x_S, y_S) = (h \sin\theta_V, L_{in} \sin\theta_H). \tag{50}$$

An initial node distribution $\mathbf{X}^0 = \{\mathbf{x}_i^0\} = \{\mathbf{x}_i^0 = (x_i^0, y_i^0)\}$ with $N = 53,961$ nodes is generated only once for the original geometry, i.e., without geometrical uncertainties, while the required node distributions $\mathbf{X} = \{\mathbf{x}_i = (x_i, y_i)\}$ for the perturbed domains are obtained by the following deformation of the initial node distribution

$$\mathbf{x}_i = \mathbf{x}_i^0 + \mathbf{x}_S \left(1 - \frac{|x_i^0|}{L_{in}}\right)\left(1 - \frac{|y_i^0|}{h}\right) \qquad \text{if } |x_i^0| < L_{in} \tag{51}$$

which shifts the step corner position of the initial node distribution $\mathbf{X}^0$ to the prescribed location $\mathbf{x}_S$ while maintaining the straightness of the step walls. We note that in this particular case, where the geometry can be mapped to the original geometry by a linear transformation with 2 random parameters, the randomness of the position of the step corner can be lifted back into the Navier-Stokes equations, allowing the construction of an accurate benchmark without the need of solving the flow problem over different geometries [74].

In order to get deeper insights on the coupling of the PC method to the RBF-FD method for the current problem, two cases will be considered: a first case with small standard deviation of the angular deviations (θ_H, θ_V) and a second case with larger standard deviation.

Case A. Both angular deviations (θ_H, θ_V) have a normal distribution with a standard deviation of 0.08 degrees, as employed in [11, 46]

$$\theta_H \sim \mathcal{N}\left(0, \left(0.08\frac{\pi}{180}\right)^2\right), \qquad \theta_V \sim \mathcal{N}\left(0, \left(0.08\frac{\pi}{180}\right)^2\right). \tag{52}$$

A convergence test for mean μ and standard deviation σ of the flow variables u, v, and p is carried out by increasing the polynomial order of the PC expansion from $P = 0$, requiring 1^2 deterministic solutions, to $P = 3$, requiring 4^2 deterministic solutions, while the reference statistical moments for the NRMSE are obtained for $P = 4$. The domain

Table 2: Stochastic flow over a backward-facing step at Re=600: mean and standard deviation normalized RMS errors (NRMSE) for flow variables u, v, p.

P	$\mu(u)$ [$\times 10^{-4}$]	$\mu(v)$ [$\times 10^{-4}$]	$\mu(p)$ [$\times 10^{-4}$]	$\sigma(u)$ [$\times 10^{-4}$]	$\sigma(v)$ [$\times 10^{-4}$]	$\sigma(p)$ [$\times 10^{-4}$]
0	0.185	0.281	1.206	-	-	-
1	0.087	0.151	0.980	3.165	3.948	8.977
2	0.031	0.047	0.277	2.747	3.389	2.919
3	0.143	0.234	0.932	2.298	3.012	6.814
4	Ref.	Ref.	Ref.	Ref.	Ref.	Ref.

Table 3: Stochastic flow over a backward-facing step at Re=600: mean and standard deviation of normalized locations of detachment and reattachment of the flow.

P	$\mu(x_1/h)$	$\mu(x_2/h)$	$\mu(x_3/h)$	$\sigma(x_1/h)$	$\sigma(x_2/h)$	$\sigma(x_3/h)$
0	10.286	8.500	15.714	-	-	-
1	10.287	8.501	15.722	$1.65{\cdot}10^{-3}$	$2.19{\cdot}10^{-2}$	0.113
2	10.286	8.501	15.714	$1.78{\cdot}10^{-3}$	$2.20{\cdot}10^{-2}$	0.117
3	10.287	8.501	15.724	$1.86{\cdot}10^{-3}$	$2.19{\cdot}10^{-2}$	0.111
4	10.286	8.501	15.714	$1.72{\cdot}10^{-3}$	$2.19{\cdot}10^{-2}$	0.118

of integration $\hat{\Omega}$ for the calculation of NRMSE in Eq. (39) is given by the intersection of each of the different deterministic domains required by the PC procedure.

The results of the convergence test are summarized in Table 2. Although the considered range for P is quite limited, from the analysis of the previous table it could be inferred that the statistical moments of each flow variable are convergent, i.e., the NRMSEs are always decreasing with P except for the case $P = 3$ which is anyway immediately below the reference case $P = 4$. We point out that this behaviour is due to the fact that the reference solution is not the exact solution, therefore the computed errors in the statistical moments are accurate only for $P \ll P_{ref} = 4$, where P_{ref} is the polynomial order P chosen for the reference solution. For this reason the computed errors in the statistical moments in the case $P = 3$ should not be considered meaningful.

Table 3 shows the convergence of mean and standard deviation of the detachment and reattachment locations, highlighting a very good estimate of the mean values already for $P = 0$, i.e., evaluating a single solution on the undeformed domain. Consistent results are also obtained for the standard deviation values, although a strong convergence is not equally evident for each of the detachment/reattachment locations.

Graphical comparisons of mean and standard deviation of the velocity magnitude $||\mathbf{u}||_2$ and pressure p are depicted in Figs. 7-10. The reference solutions are taken from [46] where the PC method is coupled with the OpenFOAM finite volume solver for the evaluation of the required deterministic responses. In both cases with RBF-FD and OpenFOAM solver, the employed PC degree is $P = 3$. The employed OpenFOAM structured mesh consists in approximately 40,000 hexahedral elements, and it is depicted in Fig. 5 where a meshless node distribution with a similar number of nodes is also depicted for comparison. Each of the contour plots of the statistical moments computed using the RBF-FD discretization, shown in Figs. 7-10, coincides, to graphical accuracy, with the corresponding reference contour plots obtained using the OpenFOAM solver.

As expected, the standard deviation of the velocity magnitude, Fig. 8, is higher in correspondence of the step

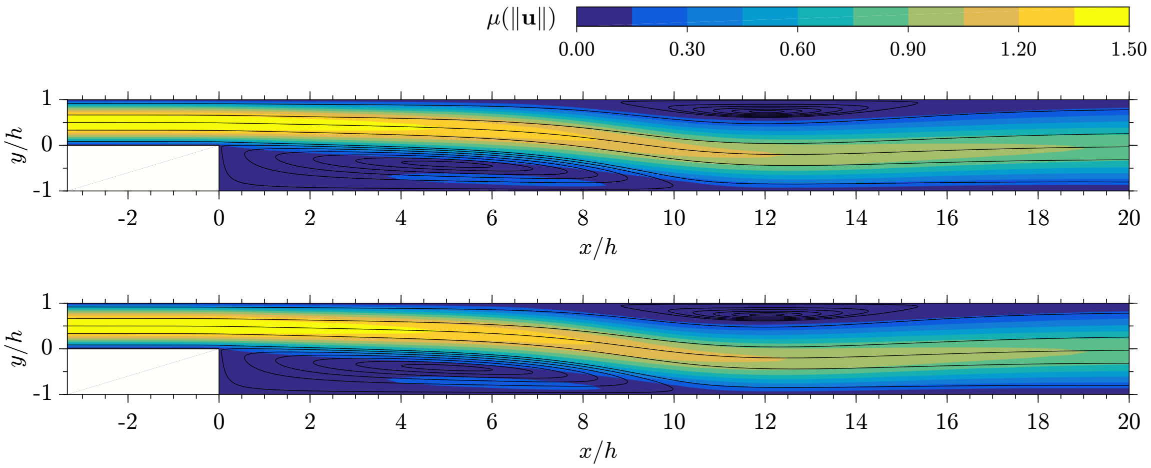

Fig. 7: Stochastic flow over a backward-facing step at Re=600, velocity mean contours: RBF-FD (top), OpenFOAM (bottom).

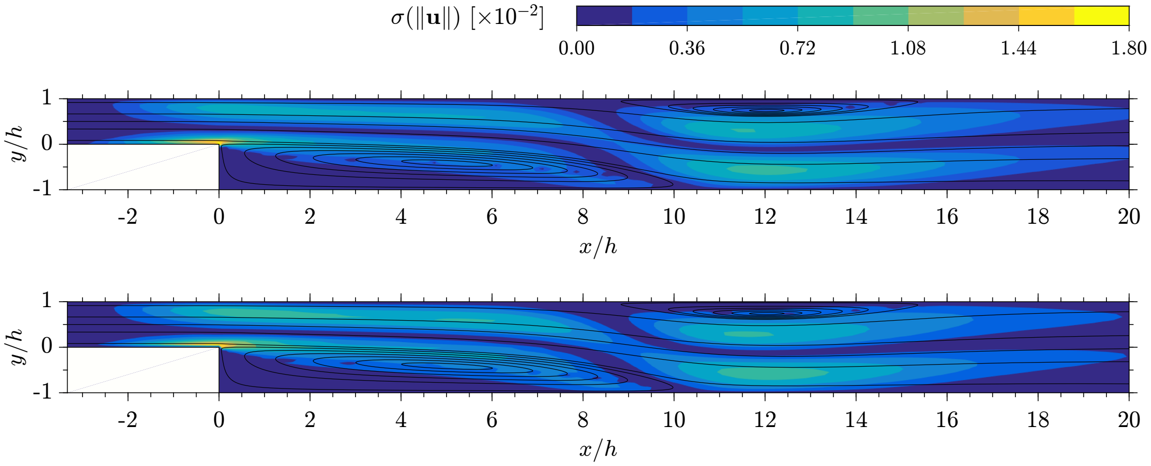

Fig. 8: Stochastic flow over a backward-facing step at Re=600, velocity standard deviation contours: RBF-FD (top), OpenFOAM (bottom).

corner and also where the flow exhibits large gradients and large velocity magnitudes at the same time. This occurs halfway between the streamline starting at the inlet at $y/h = 1/2$ (median streamline) and the limit streamlines starting at the inlet at $y \to 0^+$ and at $y/h \to 1^-$. The standard deviation of the pressure, Fig. 10, is lower near the reattachment point of the lower recirculation bubble and higher at the inlet in the neighbourhood of the horizontal step wall, as expected.

Case B. Both angular deviations (θ_H, θ_V) have a normal distribution with a standard deviation of 1.0 degree, therefore one order of magnitude larger than case A

$$\theta_H \sim \mathcal{N}\left(0, \left(\frac{\pi}{180}\right)^2\right), \qquad \theta_V \sim \mathcal{N}\left(0, \left(\frac{\pi}{180}\right)^2\right). \tag{53}$$

A convergence test for mean μ and standard deviation σ of the flow variables u, v, and p is carried out by increasing the polynomial order of the PC expansion from $P = 0$, requiring 1^2 deterministic solutions, to $P = 4$, requiring 5^2 deterministic solutions, while the reference statistical moments for the NRMSE are obtained for $P = 5$. The domain

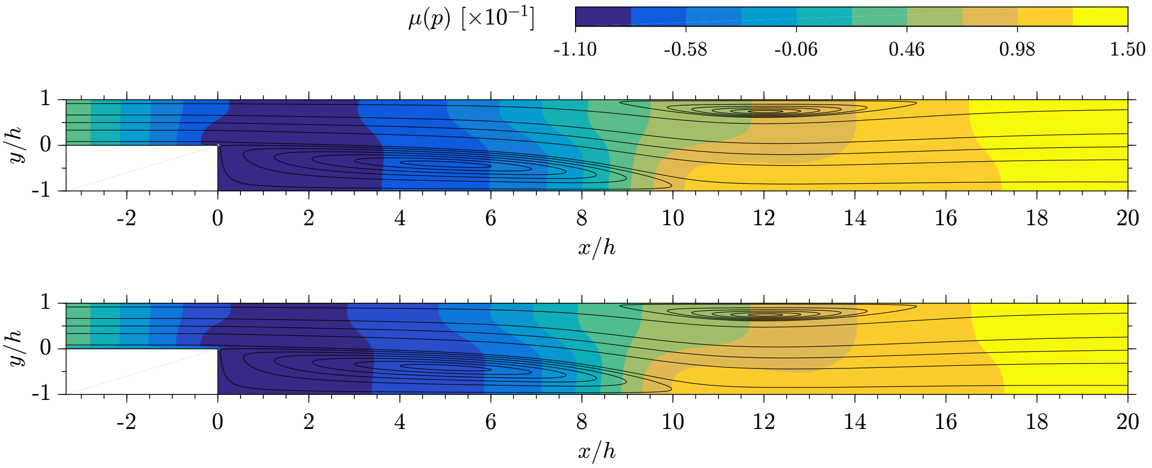

Fig. 9: Stochastic flow over a backward-facing step at Re=600, pressure mean contours: RBF-FD (top), OpenFOAM (bottom).

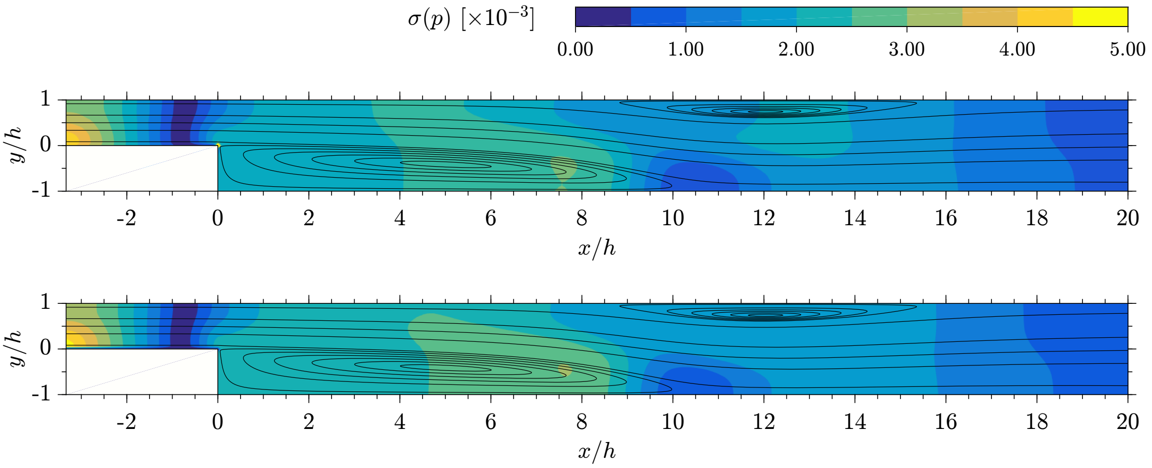

Fig. 10: Stochastic flow over a backward-facing step at Re=600, pressure standard deviation contours: RBF-FD (top), OpenFOAM (bottom).

Table 4: Stochastic flow over a backward-facing step at Re=600: mean and standard deviation normalized RMS errors (NRMSE) for flow variables u, v, p.

P	$\mu(u)$ [$\times10^{-2}$]	$\mu(v)$ [$\times10^{-2}$]	$\mu(p)$ [$\times10^{-2}$]	$\sigma(u)$ [$\times10^{-2}$]	$\sigma(v)$ [$\times10^{-2}$]	$\sigma(p)$ [$\times10^{-2}$]
0	0.759	2.888	3.198	-	-	-
1	0.173	0.299	0.062	2.201	1.422	3.609
2	0.244	0.178	0.102	1.273	0.356	0.250
3	0.040	0.165	0.024	0.897	0.194	0.077
4	0.183	0.179	0.078	1.510	0.252	0.127
5	Ref.	Ref.	Ref.	Ref.	Ref.	Ref.

of integration $\hat{\Omega}$ for the calculation of NRMSE in Eq. (39) is again given by the intersection of each of the different deterministic domains required by the PC procedure.

The results of the convergence test are summarized in Table 4: the convergence of the statistical moments of the flow variables is still present since all NRMSEs decrease when compaing $P = 1$ and $P = 3$, but it is not monotone, i.e., the NRMSEs are not always decreasing with P. Similarly to Case A, NRMSEs increase for the case $P = 4$ which

Table 5: Stochastic flow over a backward-facing step at Re=600: mean and standard deviation of normalized locations of detachment and reattachment of the flow.

P	$\mu(x_1/h)$	$\mu(x_2/h)$	$\mu(x_3/h)$	$\sigma(x_1/h)$	$\sigma(x_2/h)$	$\sigma(x_3/h)$
0	10.286	8.499	15.715	-	-	-
1	10.263	8.548	15.700	$1.10 \cdot 10^{-1}$	$1.66 \cdot 10^{-1}$	1.429
2	10.264	8.558	15.690	$1.33 \cdot 10^{-1}$	$1.98 \cdot 10^{-1}$	1.459
3	10.265	8.555	15.692	$1.32 \cdot 10^{-1}$	$2.05 \cdot 10^{-1}$	1.466
4	10.265	-	-	$1.27 \cdot 10^{-1}$	-	-
5	10.266	-	-	$1.31 \cdot 10^{-1}$	-	-

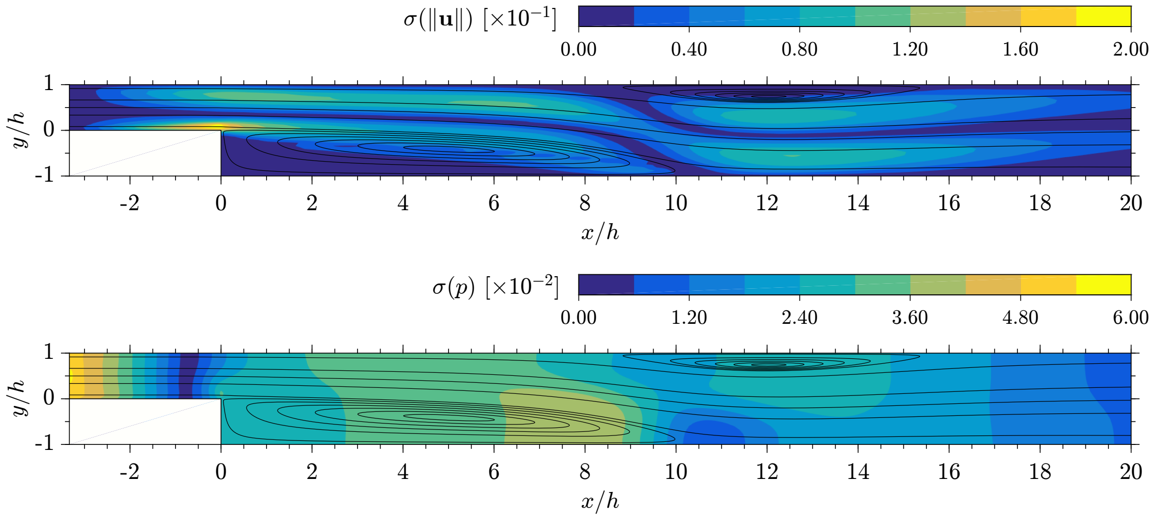

Fig. 11: Stochastic flow over a backward-facing step at Re=600, standard deviation contours: velocity (top), pressure (bottom).

is immediately below the reference case $P = 5$.

Table 5 shows the convergence of mean and standard deviation of the detachment and reattachment locations. Contrary to Case A, a PC degree $P > 0$ is needed to obtain an accurate estimate of the mean values, as expected, since the standard deviation of the uncertain parameters (θ_H, θ_V) is higher than Case A. The statistical moments of x_2 and x_3 are not available for $P = 4$ and $P = 5$ because some of the required deterministic solutions did not exhibit the upper recirculation bubble. This is expectable since for $P \geq 3$ the horizontal step wall sustains a significant deviation from the horizontal direction for some of the required configurations, preventing the formation of the upper recirculation bubble. Analogously to Case A, consistent results are obtained for the standard deviation values, although a strong convergence is not equally evident for each of the detachment/reattachment locations.

The contour plots of standard deviation of the velocity magnitude $\|\mathbf{u}\|_2$ and pressure p are depicted in Fig. 11: by a graphical comparison they appear qualitatively similar to the contour plots of Case A, Figs. 8 and 10, although the scales are different, with an exception for the standard deviation of the pressure which is higher along the whole inlet and not only near the horizontal step wall.

4.3. Nanofluid laminar flow in a microchannel

Nanofluids are regarded as an effective cooling medium with tremendous potential in heat transfer enhancement. In reality, nanofluids in microchannels are at the mercy of uncertainties unavoidably due to manufacturing error, dispersion of physical properties, and inconstant operating conditions. To obtain a deeper understanding of forced convection of nanofluids in microchannels, uncertainties are suggested to be considered. The uncertain forced convection of Al_2O_3-water nanofluid laminar flow in a grooved microchannel is numerically investigated in this section.

4.3.1. Geometry and boundary conditions

The geometry of the problem is taken from [75] and is shown in Fig. 12: the fluid enters a channel of height H at the left inlet with a prescribed parabolic profile with average velocity U_0 and temperature T_c. Adiabatic BCs are imposed at the entrance section, $x < L_1$, and at the exit section, $x > L_1 + L_2$, while a fixed temperature T_h is imposed at the boundary of the middle section, $L_1 \leq x \leq L_1 + L_2$. The reference temperature scale is chosen to be $\Delta T = T_h - T_c$. Completely developed flow BCs are imposed at the outlet, i.e., $\partial \mathbf{u}/\partial x = \mathbf{0}$, $\partial T/\partial x = 0$ and $p = 0$ are imposed. The geometrical parameters of the microchannel are listed in Table 6.

4.3.2. Physical properties

The physical properties of the Al_2O_3-water nanofluid can be expressed as functions of the solid volume fraction χ, i.e., the volume fraction of Al_2O_3. The density of the nanofluid ρ_n is therefore

$$\rho_n = (1 - \chi)\rho_w + \chi\rho_p, \tag{54}$$

where the subscripts n, w and p denote the properties of nanofluid, water and Al_2O_3, respectively. The specific heat capacity of the nanofluid c_n is

$$c_n = \frac{(1 - \chi)\rho_w c_w + \chi\rho_p c_p}{\rho_n}. \tag{55}$$

The employed model for the viscosity μ_n is [76]

$$\mu_n = \mu_w \left(123\chi^2 + 7.3\chi + 1\right) \tag{56}$$

and the employed model for the thermal conductivity k_n is [77]

$$k_n = \frac{\Delta + \sqrt{\Delta^2 + 8k_w k_p}}{4}, \tag{57}$$

where $\Delta = (2 - 3\chi)k_w + (3\chi - 1)k_p$. Ultimately, the solid volume fraction χ enters into the governing equations uniquely by means of the constant Prandtl number $\mathrm{Pr} = \mathrm{Pr}(\chi)$ in Eq. 3. The employed physical properties of water and Al_2O_3 nanoparticle are reported in Table 7 and are the same used in [75].

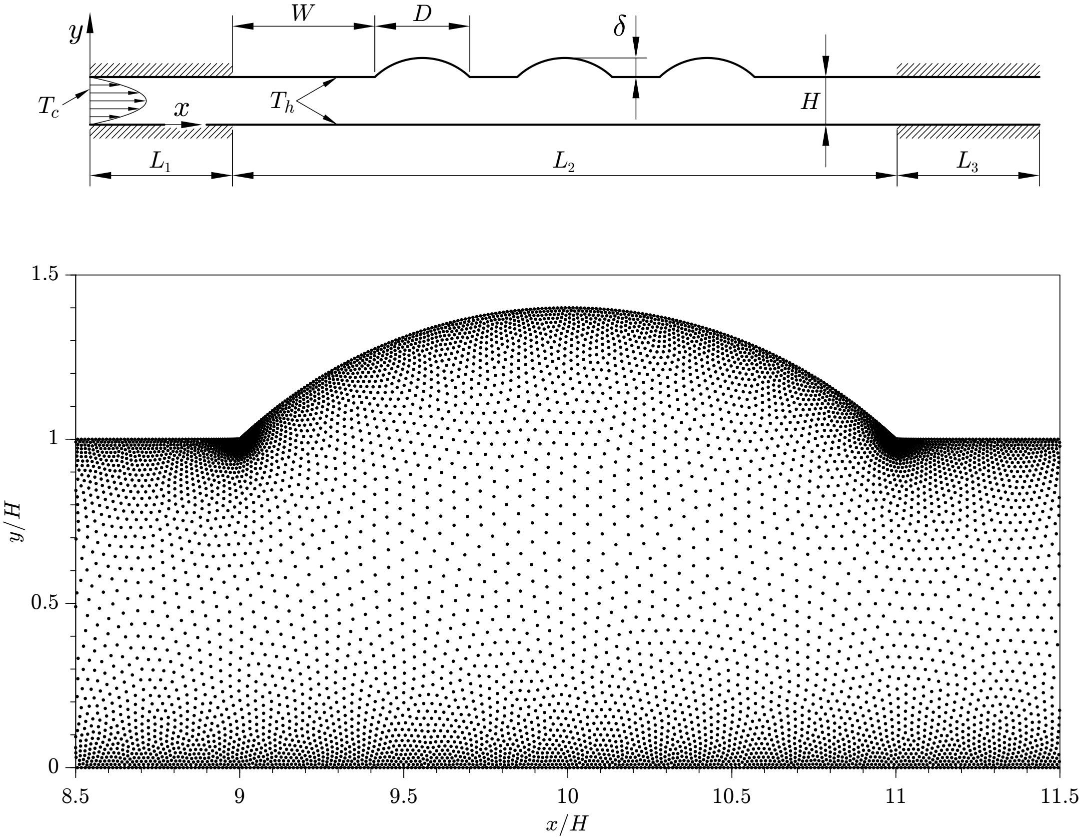

Fig. 12: Scheme of the microchannel (top) and particular of the node distribution with $N = 53,524$ nodes (bottom).

4.3.3. *Spacing function*

Similarly to the case of the backward-facing step, the spacing function for node generation is obtained by combining two contributions: the increase of the node density at the walls and a localized increase of the node density at the groove corners, i.e., at the intersection of the grooves with the horizontal walls, and at the boundary interface between the entrance, middle and exit sections, i.e., $x = L_1$ and $x = L_1 + L_2$, for a better resolution of the velocity and temperature gradients, respectively. The former contribution is expressed by Eq. (46), while the latter is expressed by factor s_2

$$s_2(\mathbf{x}) = \prod_{i=1}^{10} \left[k_S + (1 - k_S) \frac{2}{\pi} \arctan(a_S z_i) \right], \tag{58}$$

where $k_S = 40$, $a_S = 5$ and $z_i = d_i/H$ where z_i and $d_i = \|\mathbf{x} - \hat{\mathbf{x}}_i\|_2$ are the nondimensional and dimensional distances from the i-th reference point $\hat{\mathbf{x}}_i$, which can be one of the 6 groove corners or one of the 4 interface points. The spacing function is then obtained by the product of the previous factors

$$s(\mathbf{x}) = s_1(\mathbf{x}) s_2(\mathbf{x}). \tag{59}$$

Table 6: Geometrical parameters of the grooved microchannel.

H $[\mu m]$	L_1 $[\mu m]$	L_2 $[\mu m]$	L_3 $[\mu m]$	δ $[\mu m]$	D $[\mu m]$	W $[\mu m]$
25	75	350	75	10	50	75

Table 7: Physical properties of water and Al_2O_3 nanoparticle.

Component	k $[W/(m \cdot K)]$	c $[J/(kg \cdot K)]$	ρ $[kg/m^3]$	μ $[Pa \cdot s]$
Water	36	773	3880	-
Al_2O_3	0.597	4182	998.2	9.93×10^{-4}

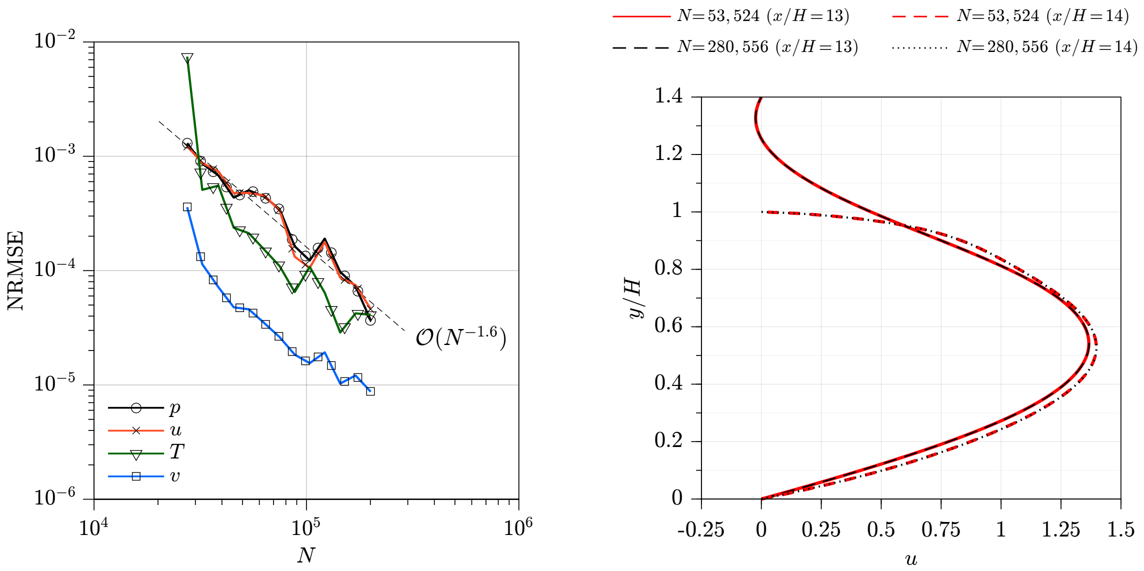

(a) (b)

Fig. 13: Deterministic flow in a microchannel at Re=100 solved by RBF-FD: normalized RMS errors vs. number of nodes N (left), comparison of u-velocity profiles (right).

An example of node distribution with $N = 53,524$ nodes is depicted in Fig. 12, where it can be observed the prescribed increase in node density at the walls and at the groove corners, according to the prescribed spacing function.

Similarly to the previous cases, polynomial degree $q = 4$ and $n = 30$ supporting nodes are always employed for the RBF-FD discretization.

4.3.4. Validation of the deterministic model

The RBF-FD solver is validated by considering the case Re = 100 and $\chi = 0.05$, i.e., 5% Al_2O_3-water nanofluid. A convergence test is carried out by increasing the total number of nodes from $N \approx 20,000$ to $N \approx 200,000$. By considering a computed solution with $N \approx 350,000$ as reference, the resulting convergence curves for the NRMSE of the velocity components (u, v), pressure p and temperature T are depicted in Fig. 13(a), where it can be observed that the resulting order of accuracy is $l = 3.2$ for each of the considered flow variables.

Table 8: Mean Nusselt number $\overline{\mathrm{Nu}}$ for the deterministic flow in a microchannel at Re=100.

N	$\overline{\mathrm{Nu}}$
27443	5.2361
32326	5.1399
38518	5.1530
45469	5.1439
53524	5.1414
63404	5.1416
74772	5.1418
88054	5.1418
103562	5.1422
121918	5.1416
144179	5.1418
170232	5.1421
200742	5.1424
237491	5.1426
280556	5.1425
∞ (extrap.)	5.1427

The convergence of the mean Nusselt number $\overline{\mathrm{Nu}}$ is reported in Table 8, where the extrapolation is obtained by a least squares fitting of the curve $c_1 + c_2 N^{-l/2}$, $l = 3.2$. Reference results of Erturk [71] are also reported in Table 1, highlighting an excellent agreement for the computed values of x_1, x_2 and x_3 with less than 1% differences.

A comparison between the u-velocity profiles for two computed solutions with $N = 53,524$ and $N = 280,556$ nodes is depicted in Fig. 13(b): the computed profiles are almost identical to graphical accuracy. Such observation is supported by the fact that the NRMSE of each flow variable is again below 10^{-3} for $N = 53,524$ nodes, Fig. 13(a). For this reason a meshless distribution with $N = 53,524$ nodes is chosen for each of the following computations.

4.3.5. Results of the stochastic model

Two uncertainties are considered: a geometric uncertainty on the depth of the grooves δ and an uncertain solid volume fraction of the nanofluid χ, both having a normal distribution with a standard deviation equal to 10% of the corresponding mean value, i.e.,

$$\delta \sim \mathcal{N}\left(\delta_0, (0.1\delta_0)^2\right), \qquad \chi \sim \mathcal{N}\left(\chi_0, (0.1\chi_0)^2\right), \tag{60}$$

where $\delta_0 = 10\mu m$ and $\chi_0 = 0.05$.

An initial node distribution $\mathbf{X}^0 = \{\mathbf{x}_i^0\} = \{\mathbf{x}_i^0 = (x_i^0, y_i^0)\}$ with $N = 53,524$ nodes is generated only once for the original geometry, while the required node distributions $\mathbf{X} = \{\mathbf{x}_i = (x_i, y_i)\}$ for the perturbed domains are obtained by the following deformation of the initial node distribution

$$y_i = y_i^0 \frac{H^\delta(x_i^0)}{H^0(x_i^0)}, \tag{61}$$

where $H^0(x)$ and $H^\delta(x)$ are the equations of the upper side of the boundary, i.e., where the grooves are placed, for the original domain and for the perturbed domain, respectively. The deformation of Eq. (61) therefore acts only on the

Table 9: Stochastic flow in a microchannel at Re=100: mean and standard deviation normalized RMS errors (NRMSE) for flow variables u, v, p, T.

P	$\mu(u)$ $[\times 10^{-3}]$	$\mu(v)$ $[\times 10^{-3}]$	$\mu(p)$ $[\times 10^{-3}]$	$\mu(T)$ $[\times 10^{-3}]$	$\sigma(u)$ $[\times 10^{-2}]$	$\sigma(v)$ $[\times 10^{-2}]$	$\sigma(p)$ $[\times 10^{-2}]$	$\sigma(T)$ $[\times 10^{-2}]$
0	0.253	0.870	0.223	1.352	-	-	-	-
1	0.023	0.031	0.045	0.059	1.162	0.665	1.246	1.104
2	0.018	0.021	0.052	0.045	0.205	0.040	0.250	0.117
3	0.003	0.005	0.004	0.019	0.039	0.015	0.112	0.019
4	0.010	0.012	0.024	0.039	0.060	0.018	0.322	0.039
5	Ref.	Ref.	Ref.	Ref.	Ref.	Ref.	Ref.	Ref.

Table 10: Stochastic flow in a microchannel at Re=100: mean and standard deviation of $\overline{\mathrm{Nu}}$.

P	0	1	2	3	4	5
$\mu(\overline{\mathrm{Nu}})$	5.140	5.146	5.146	5.147	5.146	5.147
$\sigma(\overline{\mathrm{Nu}})$ $[\times 10^{-2}]$	-	5.825	5.835	5.793	5.815	5.793

nodes below the grooves, i.e., $0 < x - (L_1 + W) < D$, $-D/2 < x - (L_1 + L_2/2) < D/2$ and $0 < x - (L_1 + L_2 - W) < D$, leaving the remaining nodes unmodified.

A convergence test for mean μ and standard deviation σ of the flow variables u, v, p and T is carried out by increasing the polynomial order of the PC expansion from $P = 0$, requiring 1^2 deterministic solutions, to $P = 4$, requiring 5^2 deterministic solutions, while the reference statistical moments for the NRMSE are obtained for $P = 5$. The domain of integration $\hat{\Omega}$ for the calculation of NRMSE in Eq. (39) is again given by the intersection of each of the different deterministic domains required by the PC procedure. The results of the convergence test are summarized in Table 9. Although the considered range for P is again limited, the analysis of the previous table suggests that the statistical moments of each flow variable are convergent, i.e., the NRMSEs are always decreasing with P except for the case $P = 4$ which is anyway immediately below the reference case $P = 5$: this behaviour has already been encountered and explained in the previous cases.

Table 10 shows the convergence of mean and standard deviation of $\overline{\mathrm{Nu}}$, highlighting that a PC degree $P = 1$ is enough for a very accurate estimate of $\mu(\overline{\mathrm{Nu}})$ which shows a convergence almost to the third decimal digit, while the values of $\sigma(\overline{\mathrm{Nu}})$ exhibit larger oscillations, although very consistent values are obtained for each P.

The contour plots of the standard deviation of the velocity magnitude $||\mathbf{u}||_2$, pressure p and temperature T are depicted in Fig. 14, Fig. 15 and Fig. 16, respectively. As expected, the standard deviation of the velocity magnitude is higher in correspondence of the downstream corners of the grooves while the upstream portion of the grooves is characterized by a recirculating bubble where the velocity magnitude is low. Similarly, the standard deviation of the pressure, Fig. 15, is higher in correspondence of the downstream corners of the grooves and also on larger zones starting from the center of the grooves. The standard deviation of the temperature, Fig. 16, exhibits a slightly different behaviour than the velocity and pressure since it is higher over an elongated zone adjacent to the boundary in the neighbourhood of the downstream portion of the grooves.

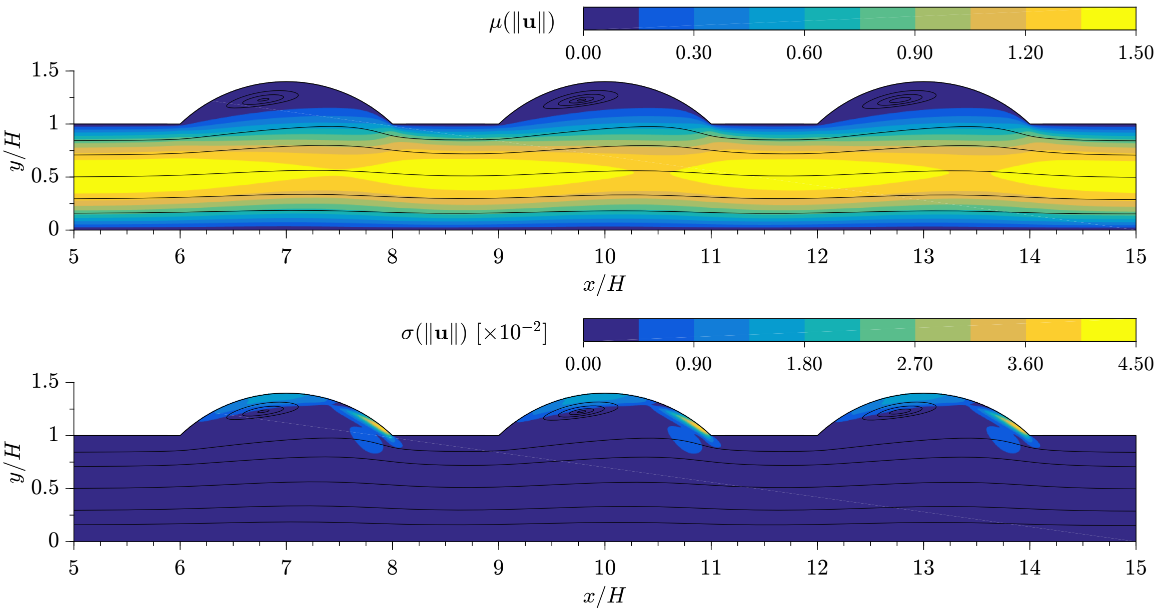

Fig. 14: Stochastic flow in a microchannel at Re=100, velocity mean (top) and standard deviation (bottom) contours.

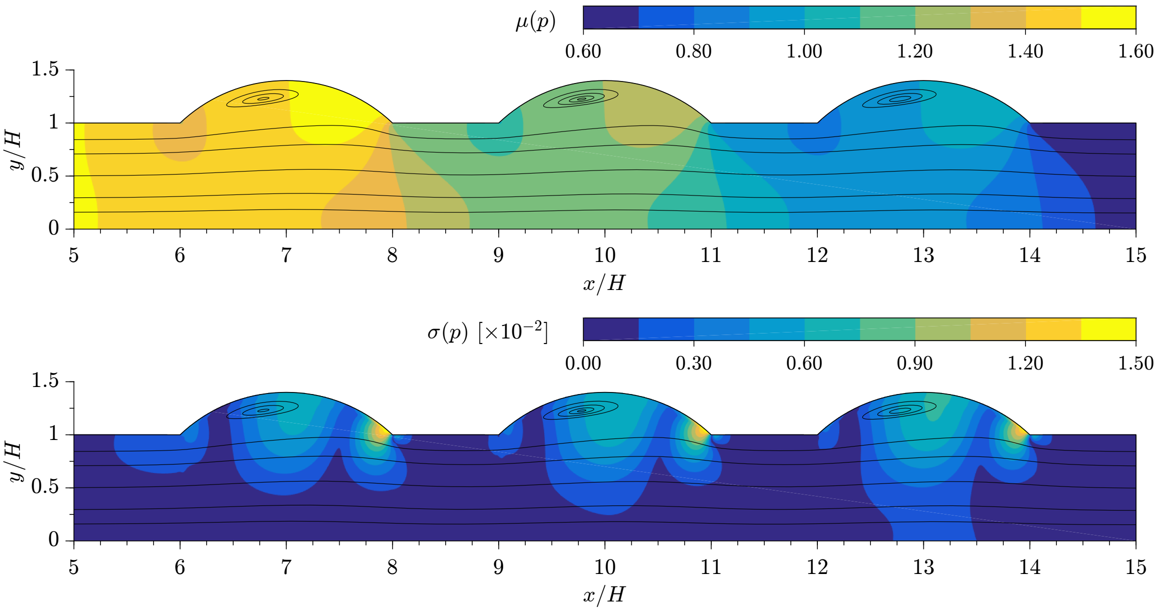

Fig. 15: Stochastic flow in a microchannel at Re=100, pressure mean (top) and standard deviation (bottom) contours.

5. Conclusions

The Non-Intrusive Polynomial Chaos method is coupled to a Radial Basis Function-generated Finite Difference meshless solver to investigate the propagation of geometric uncertainties in incompressible and laminar fluid flows. The geometric flexibility of the RBF-FD meshless method represents a great advantage over mesh-based methods when dealing with complex-shaped domains, and this feature is proven to be even more beneficial when the RBF-FD method is coupled to the PC method for the prediction of the propagation of the geometric uncertainties of the

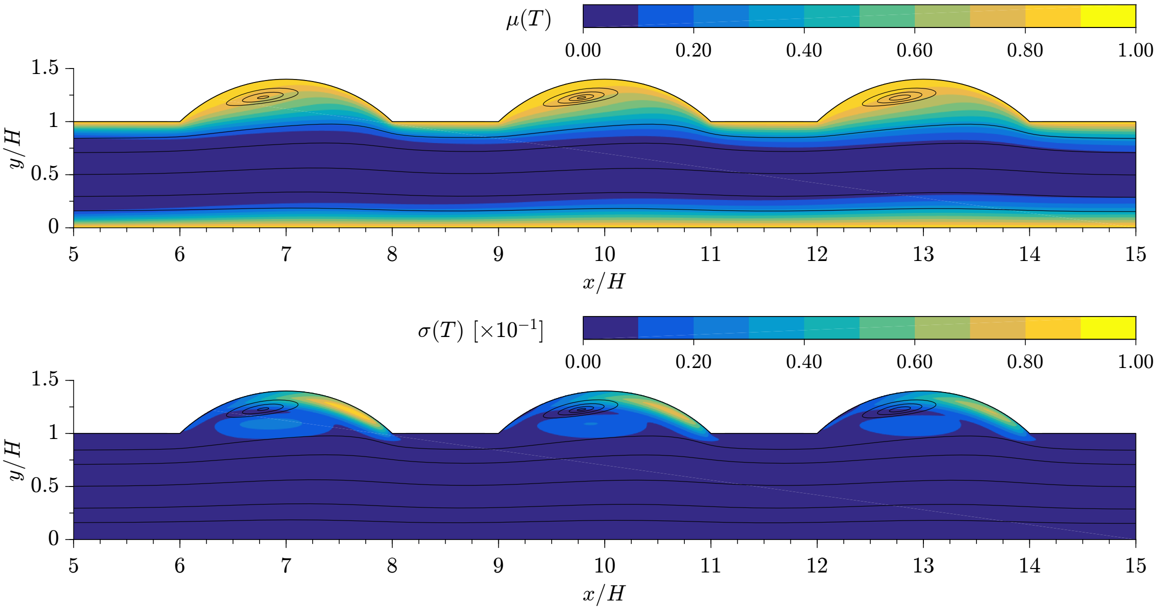

Fig. 16: Stochastic flow in a microchannel at Re=100, temperature mean (top) and standard deviation (bottom) contours.

boundaries. The capabilities of this novel approach are demonstrated through several test cases with both theoretical relevance (Wannier flow, bacward-facing step) and practical relevance (forced convection of nanofluid in a grooved microchannel), for which rigorous numerical validations are succesfully carried out. The coupling of the PC method to the RBF-FD method represents therefore an innovative, efficient and practical strategy for the accurate quantification of the fluid-flow uncertainties, especially when geometric uncertainties are defined on the boundaries.

Appendix A. Wannier flow

The Wannier flow is a two-dimensional Stokes flow past a rotating circular cylinder next to a moving wall, as depicted in Fig. 1(a) together with the cartesian coordinate system whose origin is at the center of the cylinder. The analytical solution, derived in [78] in terms of the cartesian components of the velocity $\mathbf{u} = (u, v)$, depends on the cylinder radius R, its rotational speed ω, the distance d from the center of the cylinder to the moving wall and the velocity of the wall U_0

$$\begin{aligned} u(x,y) = U_0 - 2(a_1 + a_0 Y_1)\left[\frac{S+Y_1}{K_1} + \frac{S-Y_1}{K_2}\right] - a_0 \ln(K_1/K_1) \\ - \frac{a_2}{K_1}\left[S + Y_2 - \frac{Y_2(S+Y_1)^2}{K_1}\right] - \frac{a_3}{K_2}\left[S - Y_2 + \frac{Y_2(S-Y_1)^2}{K_2}\right], \end{aligned} \tag{A.1}$$

$$v(x,y) = \frac{2x}{K_1 K_2}(a_1 + a_0 Y_1)(K_2 - K_1) - \frac{x a_2 Y_2 (S+Y_1)}{K_1^2} - \frac{x a_3 Y_2 (S-Y_1)}{K_2^2}, \tag{A.2}$$

where

$$
\begin{aligned}
&S = \sqrt{d^2 - R^2}, && \Upsilon = \frac{d+S}{d-S}, && a_0 = U_0 / \ln \Upsilon, && \\
&a_\omega = a_0 + \frac{\omega R^2}{2S}, && a_1 = -a_\omega d, && a_2 = 2(d+S)a_\omega, && a_3 = 2(d-S)a_\omega, \\
&Y_1(y) = y + d, && Y_2(y) = 2Y_1, && K_1(x,y) = x^2 + (S + Y_1)^2, && K_2(x,y) = x^2 + (S - Y_1)^2.
\end{aligned}
$$

References

[1] S. Chinchalkar, D. Taylor, Geometric uncertainties in finite element analysis, Comput. Syst. Eng. 5 (1994) 159–170.

[2] D. Xiu, G. E. Karniadakis, The Wiener–Askey polynomial chaos for stochastic differential equations, SIAM J. Sci. Comput. 24 (2002) 619–644.

[3] D. Xiu, G. E. Karniadakis, A new stochastic approach to transient heat conduction modeling with uncertainty, Int. J. Heat Mass Tran. 46 (2003) 4681–4693.

[4] O. Le Matre, O. Knio, H. Najm, R. Ghanem, Uncertainty propagation using Wiener–Haar expansions, J. Comput. Phys. 197 (2004) 28–57.

[5] D. Xiu, D. M. Tartakovsky, Numerical methods for differential equations in random domains, SIAM J. Sci. Comput. 28 (2006) 1167–1185.

[6] S. Hosder, R. Walters, R. Perez, A non-intrusive polynomial chaos method for uncertainty propagation in CFD smulations, in: 44th AIAA Aerospace Sciences Meeting and Exhibit, American Institute of Aeronautics and Astronautics, Reston, Virigina, 2006, pp. 2006–2891. URL: `http://arc.aiaa.org/doi/10.2514/6.2006-891`. doi:10.2514/6.2006-891.

[7] G. Lin, C.-H. Su, G. Karniadakis, Modeling random roughness in supersonic flow past a wedge, in: 44th AIAA Aerospace Sciences Meeting and Exhibit, American Institute of Aeronautics and Astronautics, Reston, Virigina, 2006, pp. 124–2006. URL: `http://arc.aiaa.org/doi/10.2514/6.2006-124`. doi:10.2514/6.2006-124.

[8] G. Loeven, J. Witteveen, H. Bijl, Probabilistic Collocation: An Efficient Non-Intrusive Approach for Arbitrarily Distributed Parametric Uncertainties, American Institute of Aeronautics and Astronautics, Reston, Virigina, 2007. URL: `http://arc.aiaa.org/doi/10.2514/6.2007-317`. doi:10.2514/6.2007-317.

[9] L. Parussini, V. Pediroda, Fictitious domain with least-squares spectral element method to explore geometric uncertainties by non-intrusive polynomial chaos method, CMES-Comp. Model. Eng. 22 (2007) 41–64.

[10] C. Canuto, T. Kozubek, A fictitious domain approach to the numerical solution of PDEs in stochastic domains, Numer. Math. 107 (2007) 257–293.

[11] L. Parussini, V. Pediroda, C. Poloni, Prediction of geometric uncertainty effects on fluid dynamics by polynomial chaos and fictitious domain method, Comput. Fluids 39 (2010) 137–151.

[12] B. S. Lazarov, M. Schevenels, O. Sigmund, Topology optimization with geometric uncertainties by perturbation techniques, Int. J. Numer. Meth. Eng. 90 (2012) 1321–1336.

[13] Q. Meng, J. Fisher, R. Wilcox, The effects of geometric uncertainties on computational modelling of knee biomechanics, Roy. Soc. Open Sci. 4 (2017) 170670.

[14] D. Quagliarella, A. Serani, M. Diez, M. Pisaroni, P. Leyland, L. Montagliani, U. Iemma, N. J. Gaul, J. Shin, D. Wunsch, C. Hirsch, K. Choi, F. Stern, Benchmarking uncertainty quantification methods using the NACA 2412 airfoil with geometrical and operational uncertainties, in: AIAA Aviation 2019 Forum, American Institute of Aeronautics and Astronautics, Reston, Virginia, 2019. URL: `https://arc.aiaa.org/doi/10.2514/6.2019-3555`. doi:10.2514/6.2019-3555.

[15] M. Eldred, Recent advances in non-intrusive polynomial chaos and stochastic collocation methods for uncertainty analysis and design, in: 50th AIAA/ASME/ASCE/AHS/ASC Structures, Structural Dynamics, and Materials Conference, American Institute of Aeronautics and Astronautics, Reston, Virigina, 2009. URL: `http://arc.aiaa.org/doi/10.2514/6.2009-2274`. doi:10.2514/6.2009-2274.

[16] B. Fornberg, N. Flyer, Solving PDEs with radial basis functions, Acta Numer. 24 (2015) 215–258.

[17] S. A. Sarra, E. J. Kansa, Multiquadric Radial Basis Function Approximation Methods for the Numerical Solution of Partial Differential Equations, volume 2 of *Advances in Comput. Mech.*, Tech Science Press, 2009. URL: `http://www.scottsarra.org/math/papers/mqMonographSarraKansa.pdf`.

[18] N. Flyer, B. Fornberg, V. Bayona, G. A. Barnett, On the role of polynomials in RBF-FD approximations: I. Interpolation and accuracy, J. Comput. Phys. 321 (2016) 21–38.

[19] V. Bayona, N. Flyer, B. Fornberg, G. A. Barnett, On the role of polynomials in RBF-FD approximations: II. numerical solution of elliptic PDEs, J. Comput. Phys. 332 (2017) 257–273.

[20] R. Zamolo, Radial Basis Function-Finite Difference Meshless Methods for CFD Problems, Ph.D. thesis, Trieste, Italy, 2019. URL: `http://hdl.handle.net/11368/2942917`.

[21] H. Li, S. S. Mulay, Meshless Methods and Their Numerical Properties, CRC Press, 2013. URL: `https://www.taylorfrancis.com/books/9781466517479`. doi:10.1201/b14492.

[22] G. Liu, Meshfree Methods, CRC Press, 2009. URL: `https://www.taylorfrancis.com/books/9781420082104`. doi:10.1201/9781420082104.

[23] E. Divo, A. J. Kassab, An efficient localized radial basis function meshless method for fluid flow and conjugate heat transfer, J. Heat Transf. 129 (2007) 124–136.

[24] E. Divo, A. J. Kassab, Localized meshless modeling of natural-convective viscous flows, Numer. Heat Tr. B-Fund. 53 (2008) 487–509.

[25] G. Kosec, B. Šarler, Solution of thermo-fluid problems by collocation with local pressure correction, Int. J. Numer. Method. H. 18 (2008) 868–882.

[26] P. P. Chinchapatnam, K. Djidjeli, P. B. Nair, M. Tan, A compact RBF-FD based meshless method for the incompressible NavierStokes equations, Proceedings of the Institution of Mechanical Engineers, Part M: Journal of Engineering for the Maritime Environment 223 (2009) 275–290.

[27] J. Waters, D. W. Pepper, Global versus localized RBF meshless methods for solving incompressible fluid flow with heat transfer, Numer. Heat Tr. B-Fund. 68 (2015) 185–203.

[28] R. Zamolo, E. Nobile, Solution of incompressible fluid flow problems with heat transfer by means of an efficient RBF-FD meshless approach, Numer. Heat Tr. B-Fund. 75 (2019) 19–42.

[29] A. J. Chorin, Numerical solution of the Navier-Stokes equations, Math. Comput. 22 (1968) 745.

[30] N. Metropolis, S. Ulam, The Monte Carlo method, J. Am. Stat. Assoc. 44 (1949) 335.

[31] C. P. Robert, G. Casella, Monte Carlo Statistical Methods, Springer Texts in Statistics, 2nd ed., Springer New York, New York, NY, 2004. URL: `http://link.springer.com/10.1007/978-1-4757-4145-2`. doi:10.1007/978-1-4757-4145-2.

[32] L. Mathelin, Y. Hussaini, A stochastic collocation algorithm for uncertainty analysis, Technical Report NASA CR-2003-212153, NASA Center: Langley Research Center, 2003. URL: `https://ntrs.nasa.gov/archive/nasa/casi.ntrs.nasa.gov/20030016674.pdf`.

[33] I. Babuška, F. Nobile, R. Tempone, A stochastic collocation method for elliptic partial differential equations with random input data, SIAM J. Numer. Anal. 45 (2007) 1005–1034.

[34] F. Nobile, R. Tempone, C. G. Webster, A sparse grid stochastic collocation method for partial differential equations with random input data, SIAM J. Numer. Anal. 46 (2008) 2309–2345.

[35] G. Loeven, J. Witteveen, H. Bijl, Efficient uncertainty quantification using a two step approach with chaos collocation, in: In Proc. ECCOMAS CFD, Delft University of Technology, Delft University of Technology, 2006. URL: `http://resolver.tudelft.nl/uuid:2b9f4315-bc5a-4767-a48f-15d5bfb6be96`.

[36] X. D., Efficient collocational approach for parametric uncertainty analysis, Commun. Comput. Phys. 2 (2007) 293–309.

[37] V. Pediroda, C. Poloni, A. Clarich, A fast and robust adaptive methodology for airfoil design under uncertainties based on game theory and self-organising-map Theory, in: 44th AIAA Aerospace Sciences Meeting and Exhibit, American Institute of Aeronautics and Astronautics, Reston, Virigina, 2006, pp. 29–36. URL: `http://arc.aiaa.org/doi/10.2514/6.2006-1472`. doi:10.2514/6.2006-1472.

[38] M. K. Deb, I. M. Babuška, J. Oden, Solution of stochastic partial differential equations using Galerkin finite element techniques, Comput. Method. Appl. M. 190 (2001) 6359–6372.

[39] R. G. Ghanem, P. D. Spanos, Stochastic Finite Elements: A Spectral Approach, Springer New York, New York, NY, 1991. URL: `http://link.springer.com/10.1007/978-1-4612-3094-6`. doi:10.1007/978-1-4612-3094-6.

[40] B. Sudret, Polynomial chaos expansions and stochastic finite element methods, CRC Press., 2014, pp. 265–300. URL: `https://hal.archives-ouvertes.fr/hal-01449883`.

[41] D. Xiu, Numerical Methods for Stochastic Computations, Princeton University Press, 2010. URL: `http://www.jstor.org/stable/10.2307/j.ctv7h0skv`. doi:10.2307/j.ctv7h0skv.

[42] M. Eldred, J. Burkardt, Comparison of non-intrusive polynomial chaos and stochastic collocation methods for uncertainty quantification, 47th AIAA Aerospace Sciences Meeting including The New Horizons Forum and Aerospace Exposition 976 (2009) 1–20.

[43] Y. M. Marzouk, H. N. Najm, Dimensionality reduction and polynomial chaos acceleration of Bayesian inference in inverse problems, J. Comput. Phys. 228 (2009) 1862–1902.

[44] J. Hampton, A. Doostan, Compressive sampling of polynomial chaos expansions: Convergence analysis and sampling strategies, J. Comput. Phys. 280 (2015) 363–386.

[45] I.-G. Farca, B. Uekermann, T. Neckel, H.-J. Bungartz, Nonintrusive uncertainty analysis of fluid-structure interaction with spatially adaptive sparse grids and polynomial chaos expansion, SIAM J. Sci. Comput. 40 (2018) B457–B482.

[46] L. Parussini, V. Pediroda, C. Poloni, A. Clarich, R. Russo, Comparison of body-fitted and fictitious domain approach for CFD prediction of geometric incertanties by polynomial chaos using modeFRONTIER, in: In Proc. EUROGEN 2011, Evolutionary and Deterministic Methods for Design, Optimization and Control with Applications to Industrial and Societal Problems, 2011, pp. 230–232. URL: `http://hdl.handle.net/11368/2376790`.

[47] R. Zamolo, E. Nobile, Two algorithms for fast 2D node generation: Application to RBF meshless discretization of diffusion problems and image halftoning, Comput. Math. Appl. 75 (2018) 4305–4321.

[48] H. Samet, The quadtree and related hierarchical data structures, ACM Comput. Surv. 16 (1984) 187–260.

[49] R. A. Ulichney, Review of halftoning techniques, in: R. Eschbach, G. G. Marcu (Eds.), Color Imaging: Device-Independent Color, Color Hardcopy, and Graphic Arts V, volume 3963, International Society for Optics and Photonics, SPIE, 1999, pp. 378–391. URL: `http://proceedings.spiedigitallibrary.org/proceeding.aspx?articleid=920677`. doi:10.1117/12.373419.

[50] G. E. Fasshauer, Meshfree Approximation Methods with Matlab, volume 6 of *Interdisciplinary Mathematical Sciences*, WORLD SCIENTIFIC, Singapore, 2007. URL: `https://www.worldscientific.com/worldscibooks/10.1142/6437`. doi:10.1142/6437.

[51] R. L. Hardy, Multiquadric equations of topography and other irregular surfaces, J. Geophys. Res. 76 (1971) 1905–1915.

[52] R. Hardy, Theory and applications of the multiquadric-biharmonic method 20 years of discovery 1968–1988, Comput. Math. Appl. 19 (1990) 163–208.

[53] R. Franke, A Critical Comparison of Some Methods for Interpolation of Scattered Data (Technical Report), Technical Report NPS-53-79-003, Naval Postgraduate School, Monterey, California, 1980. URL: `http://hdl.handle.net/10945/35052`.

[54] R. Franke, Scattered data interpolation: tests of some methods, Math. Comput. 38 (1982) 181–181.

[55] T. Driscoll, B. Fornberg, Interpolation in the limit of increasingly flat radial basis functions, Comput. Math. Appl. 43 (2002) 413–422.

[56] R. A. Horn, C. R. Johnson, Matrix Analysis, 2nd ed., Cambridge University Press, 1990. URL: `http://www.cse.zju.edu.cn/eclass/attachments/2015-10/01-1446086008-145421.pdf`.

[57] F. H. Harlow, J. E. Welch, Numerical calculation of timedependent viscous incompressible flow of fluid with free surface, Phys. Fluids 8 (1965) 2182–2189.

[58] R. L. Sani, P. M. Gresho, R. L. Lee, D. F. Griffiths, The cause and cure (?) of the spurious pressures generated by certain FEM solutions of the incompressible Navier-Stokes equations: Part 1, Int. J. Numer. Meth. Fl. 1 (1981) 17–43.

[59] R. L. Sani, P. M. Gresho, R. L. Lee, D. F. Grifftths, M. Engelman, The cause and cure (!) of the spurious pressures generated by certain fem solutions of the incompressible Navier-Stokes equations: Part 2, Int. J. Numer. Meth. Fl. 1 (1981) 171–204.

[60] C. M. Rhie, W. L. Chow, Numerical study of the turbulent flow past an airfoil with trailing edge separation, AIAA J. 21 (1983) 1525–1532.

[61] B. Koren, Upwind schemes for the Navier-Stokes equations, Vieweg+Teubner Verlag, Wiesbaden, 1989, pp. 300–309. URL: `http://link.springer.com/10.1007/978-3-322-87869-4_31`. doi:10.1007/978-3-322-87869-4_31.

[62] Y. T. Gu, G. R. Liu, Meshless techniques for convection dominated problems, Comput. Mech. 38 (2006) 171–182.

[63] G. Chandhini, Y. V. S. S. Sanyasiraju, Local RBF-FD solutions for steady convection-diffusion problems, Int. J. Numer. Meth. Eng. 72 (2007) 352–378.

[64] D. Yun, Y. Hon, Improved localized radial basis function collocation method for multi-dimensional convection-dominated problems, Eng. Anal. Bound. Elem. 67 (2016) 63–80.

[65] P. K. Mishra, G. E. Fasshauer, M. K. Sen, L. Ling, A stabilized radial basis-finite difference (RBF-FD) method with hybrid kernels, Comput. Math. Appl. 77 (2019) 2354–2368.

[66] B. Fornberg, E. Lehto, Stabilization of RBF-generated finite difference methods for convective PDEs, J. Comput. Phys. 230 (2011) 2270–2285.

[67] H. A. van der Vorst, Bi-CGSTAB: A fast and smoothly converging variant of Bi-CG for the solution of nonsymmetric linear systems, SIAM J. Sci. Stat. Comp. 13 (1992) 631–644.

[68] Y. Saad, Iterative Methods for Sparse Linear Systems, 2nd ed., Society for Industrial and Applied Mathematics, Philadelphia, Pennsylvania, 2003, pp. 297–368. URL: `http://epubs.siam.org/doi/book/10.1137/1.9780898718003`. doi:10.1137/1.9780898718003.

[69] D. L. Brown, R. Cortez, M. L. Minion, Accurate projection methods for the incompressible Navier–Stokes equations, J. Comput. Phys. 168 (2001) 464–499.

[70] L. Chen, K. Asai, T. Nonomura, G. Xi, T. Liu, A review of backward-facing step (BFS) flow mechanisms, heat transfer and control, Therm. Sci. Eng. Proc. 6 (2018) 194–216.

[71] E. Erturk, Numerical solutions of 2-D steady incompressible flow over a backward-facing step, Part I: High Reynolds number solutions, Comput. Fluids 37 (2008) 633–655.

[72] T. Lee, D. Matescu, Experimental and numerical investigation of 2-D backward-facing step flow, J. Fluid. Struct. 12 (1998) 703–716.

[73] B. F. Armaly, F. Durst, J. C. F. Pereira, B. Schönung, Experimental and theoretical investigation of backward-facing step flow, J. Fluid. Mech. 127 (1983) 473–496.

[74] H. Luo, T. R. Bewley, On the contravariant form of the Navier–Stokes equations in time-dependent curvilinear coordinate systems, J. Comput. Phys. 199 (2004) 355–375.

[75] Z. Zheng, Q. Jing, Y. Xie, D. Zhang, An investigation on the forced convection of Al2O3-water nanofluid laminar flow in a microchannel under interval uncertainties, Appl. Sci.-Basel 9 (2019) 432.

[76] S. E. B. Maïga, S. J. Palm, C. T. Nguyen, G. Roy, N. Galanis, Heat transfer enhancement by using nanofluids in forced convection flows, Int. J. Heat Fluid Fl. 26 (2005) 530–546.

[77] O. Mahian, A. Kianifar, C. Kleinstreuer, M. A. Al-Nimr, I. Pop, A. Z. Sahin, S. Wongwises, A review of entropy generation in nanofluid flow, Int. J. Heat Mass Tran. 65 (2013) 514–532.

[78] G. H. Wannier, A contribution to the hydrodynamics of lubrication, Q. Appl. Math. 8 (1950) 1–32.